Published in final edited form as:
Acta Biomater. 2020 January 15; 102: 149–168. doi:10.1016/j.actbio.2019.11.028.

Integration of polarized spatial frequency domain imaging (pSFDI) with a biaxial mechanical testing system for quantification of load-dependent collagen architecture in soft collagenous tissues

Samuel V. Jett[1], **Luke T. Hudson**[1], **Ryan Baumwart**[2], **Bradley N. Bohnstedt**[3,*], **Arshid Mir**[4], **Harold M. Burkhart**[5], **Gerhard A. Holzapfel**[6,7], **Yi Wu**[1], **Chung-Hao Lee**[1,8]

[1]Biomechanics and Biomaterials Design Laboratory, School of Aerospace and Mechanical Engineering, The University of Oklahoma

[2]Center for Veterinary Health Sciences, Oklahoma State University

[3]Department of Neurosurgery, The University of Oklahoma Health Sciences Center

[4]Division of Pediatric Cardiology, Department of Pediatrics, The University of Oklahoma Health Sciences Center

[5]Division of Cardiothoracic Surgery, Department of Surgery, The University of Oklahoma Health Sciences Center

[6]Institute of Biomechanics, Graz University of Technology

[7]Department of Structural Engineering, Norwegian University of Science and Technology (NTNU)

[8]Institute for Biomedical Engineering, Science and Technology, The University of Oklahoma

Abstract

Collagen fiber networks provide the structural strength of tissues such as tendons, skin, and arteries. Quantifying the response of the fiber architecture to mechanical loads is essential towards a better understanding of the tissue-level mechanical behaviors, especially in assessing disease-driven functional changes. To enable novel investigations into these *load-dependent* fiber structures, a polarized spatial frequency domain imaging (pSFDI) device was developed and, *for the first time*, integrated with a biaxial mechanical testing system. The integrated instrument is capable of a wide-field quantification of the fiber orientation and degree of optical anisotropy (DOA), representing the local degree of fiber alignment. The opto-mechanical instrument's performance was assessed through uniaxial loading on tendon tissues with known collagen fiber microstructures. Our results revealed that the bulk fiber orientation angle of the tendon tissue changed minimally with loading (median±0.5*IQR of 52.7°±3.3° and 51.9°±3.3° under 0 and 3%

For correspondence: Chung-Hao Lee, Ph.D., Assistant Professor, School of Aerospace and Mechanical Engineering, Affiliated Faculty Member, Institute for Biomedical Engineering, Science, and Technology, The University of Oklahoma, 865 Asp Ave., Felgar Hall Rm. 219C, Norman OK 73019-3609, ch.lee@ou.edu; Tel: +1-405-325-4842.
*Present Affiliation: Department of Neurological Surgery, Indiana University School of Medicine

Conflicts of Interest
The authors of this paper have no financial or personal relationships with other people or organizations that could inappropriately influence (bias) our work.

longitudinal strains, respectively), whereas on a micro-scale the fibers became better aligned with the direction of loading: the DOA (mean±SD) increased from 0.149±0.032 to 0.198±0.056 under 0 and 3% longitudinal strains, respectively, $p<0.001$. The integrated instrument was further applied to study two representative mitral valve anterior leaflet (MVAL) tissues subjected to various biaxial loads. The fiber orientations within these representative MVAL tissue specimens demonstrated noticeable heterogeneity, with local fiber orientations dependent upon the sample, the spatial and transmural locations, and the applied loading. Our results also showed that fibers were generally better aligned under equibiaxial (DOA=0.089±0.036) and circumferentially-dominant loading (DOA=0.086±0.037) than under the radially-dominant loading (DOA=0.077±0.034), indicating circumferential predisposition. These novel findings exemplify a deeper understanding of the load-dependent collagen fiber microstructures obtained through the use of the integrated opto-mechanical instrument.

Keywords

collagen fiber architecture; microstructure; quantitative optical technique; polarization imaging; biaxial loading; heart valve; load-dependence

1. Introduction

Collagen fibers comprise the extracellular matrix (ECM) in soft collagenous tissues, such as tendons, arteries, heart valve leaflets and skin. In collagenous tissues like these, the fibers are arranged in specific architectures to support the functional requirements of the native biological material. Owing to the essential relationship between tissue's mechanical function and collagen fiber organization, significant efforts have been dedicated to examinations of the collagen fibers architectures (CFAs) in various tissues [1–3]. These research studies have traditionally analyzed tissues – either tissues not subjected to external mechanical loading or tissues chemically fixed at specific mechanical loads. For example, existing studies have reported the orientation and spread of collagen fibers throughout the unloaded sclera, meniscus, and murine lung, among others [4–6]. However, these quantifications, considering tissues not subjected to mechanical load, may be inadequate for understanding the CFA's contribution to the overall mechanical function of the tissue, because collagen networks change in response to mechanical loads [7–9]. Moreover, computational models oftentimes employ an affine fiber kinematic assumption to describe these collagen network changes in response to mechanical loading (see, e.g., [10–12]), but validation of this modeling assumption would require more experimental knowledge regarding load-dependent collagen fiber architectural database that is currently limited in the literature. Thus, an improved description of the fiber architecture and its relation to tissue-level and organ-level function could be obtained by quantifications of changes to fiber networks under applied mechanical loading. Such combined structural and mechanical descriptions of the load-dependent fiber architecture are essential for establishing the structure-function relationship in healthy tissues, and for improving the understanding of structural and functional degradation in tissue diseases, including tears in tendon, arterial aneurysms, aortic dissections, and stenosis or calcification in heart valve leaflets (such as [13–18]).

Several collagen microstructural imaging techniques (Table 1) have been developed and widely employed in the context of identifying the microstructure of soft collagenous tissues, including polarized spatial frequency domain imaging (pSFDI) [19, 20], quantitative-polarized light microscopy (Q-PLM) [21, 22], small angle scattering techniques (small angle light scattering (SALS) and small angle X-ray Scattering (SAXS)) [23–25], second harmonic generation (SHG) microscopy [26–29], confocal microscopy methods, especially laser scanning confocal microscopy (LSCM) [30], and standard histological methods [31, 32]. Each of these imaging techniques provides a unique means to examine the collagen fiber structure with their own distinct proficiencies and shortcomings. For example, on the one hand, pSFDI, SALS, and some recent implementations of Q-PLM can provide quantifications of the fiber structure over a large field of view (FOV), but as they consider *aggregated* signals from scattering events within a sample, the signal from collagen fibers can be masked by scattering from other microstructural constituents. On the other hand, standard Q-PLM, SHG imaging, LSCM, and microscopy of histological samples provide more concrete methods to ensure that only the collagen fibers are examined through visualization of individual fibers; however, through the increased resolution, large FOV measurements, typically the entire tissue sample spatially and transmurally, may not be feasible. Moreover, SALS and Q-PLM techniques often times require alterations to the tissue, such as optical clearing techniques or histological sectioning and staining. Such alterations provide an improved resolution and contrast of the CFA in the tissue, but, in the meantime, remove any ability to assess the *functional*, load-dependent changes in the collagen microstructure in response to physiological loading. In contrast, techniques, such as confocal microscopy and pSFDI, show great potential for assessing the load-dependent CFAs in collagenous tissue samples [33–35]: Confocal microscopy methods have been employed to noninvasively examine cross-linking in corneal and skin collagen fiber structures *in vivo* and under loading states [36, 37]. Nevertheless, pSFDI techniques have yet to be used towards analyses of the load-dependent collagen structures in soft collagenous tissues.

The information presented in Table 1 confers a baseline for each systems' capabilities, as the imaging techniques have been frequently customized and extended for specific research applications, yielding a variety of FOVs, imaging resolutions, and image acquisition times. For example, although polarized light microscopy is traditionally used to examine histologically-prepared samples on a microscopic scale, techniques were recently applied, via the addition of quarter-wave plates, to examine the load-dependent collagen structures in the tendon-insertion attachment over a cm-scale in milliseconds, albeit with a lower spatial resolution [38]. Similarly, a modified Q-PLM system was developed to semi-quantitatively examine the load-dependent collagen structures in a tissue sample under uniaxial loading [39]. In another custom application, a commercial SHG device was integrated with a mechanical testing system to examine changes to collagen fibril structures in pericardial tissues under biaxial mechanical loads [40]. For the arterial tissues, recent studies combined SALS [41] or confocal microscopy [42] with mechanical loading techniques to gain a high-resolution, narrow FoV understanding of collagen fiber extension and changes in the individual fiber's tortuosity. The devices used in these studies and similar in [43] are especially valuable for characterizing the collagen mechanical behavior in tissues that can be

assumed spatially homogenous; for other collagenous tissues, such as the cardiac heart valve leaflets, microstructural heterogeneities may not permit extrapolation of the measured CFSs, thus limiting the applicability of such collagen fiber characterizations for finite element modeling.

Similarly, previous studies have used light scattering techniques to effectively examine the load-dependent kinematics of collagen molecular and fibrillar structures at a nm-scale using SAXS [25, 44], or the load-dependent behavior of the larger-scale fibers through SALS [45, 46]. However, these transmissive light scattering-based techniques are unable to discriminate the scattering contributions from each layer in the transmurally-heterogenous tissue samples. In the heart valve leaflet tissues, such layer-specific microstructural characterizations have traditionally been possible only through destructive histological sectioning techniques [47]. On the other hand, the pSFDI technique was recently used for quantitative analyses of the collagen fiber orientation and degree of alignment across the distinct morphological layers of the native aortic valve tissues at the unloaded state, providing a valuable understanding of transmural variance in collagen fiber arrangement [35].

As detailed in the previous paragraphs, imaging techniques have yielded broad capabilities toward investigating soft collagenous tissue's microstructures [48]. Despite the recent advances, no viable device has yet been reported to allow monitoring the load-dependent CFAs in tissues subjected to arbitrary external mechanical loadings or provided rigorous quantifications of the CFAs over a tissue-scale FOV (spatial and transmural). This shortcoming underscores the lack of understanding of how the collagen fiber microstructure changes and reorients to support the functional mechanical behavior and, conversely, how the heterogenous alterations to the load-dependent CFA may contribute to tissue-level diseases. To provide this much needed analytical capability, the overall goal of this study is first to develop a pSFDI device, and to further integrate this device with a commercial biaxial mechanical tester. The integrated system is capable of depth-modulated quantifications of collagen fiber orientation and degree of alignment throughout the spatial and transmural domain of a tissue sample. In addition, the integrated instrument allows quantifications of the CFAs in tissue samples subjected to biaxial loading, rendering a novel and essential tool for opto-mechanical analyses of collagenous tissues, such as heart valve leaflets, arteries and skin. The performance of the integrated instrument was assessed through combined mechano-structural testing on bovine tendon tissues with a known CFA [49]. Finally, the instrument was utilized to examine the load-dependent, heterogenous CFAs in the mitral valve anterior leaflet (MVAL) tissues in the physiologically-relevant environment.

2. Methods

2.1 Overview on the theory of birefringent collagen scattering

When subjected to polarized illumination, collagen fibers exhibit birefringence, i.e., a refractive response that depends upon the polarization and propagation of the incident light. More specifically, collagen fibers manifest a *structural* birefringence arising from the cylindrical shape of the fibers. The structural birefringence can be captured via a *co-polarization* imaging approach, which is a reflectance-based imaging methodology wherein

both the light approaching a sample and the reflected light from the sample pass through the same linear polarizer with an angle $\theta_{polarizer}$. This co-polarized imaging system can be realized with several optical components (Fig. 1a), including a light projector, a linear polarizer, and a CCD camera.

By incrementally rotating the polarizer in a co-polarized imaging system from 0° to 180° and sequentially capturing the corresponding reflected intensity associated with each $\theta_{polarizer}$, the birefringence of the collagen structure causes variation in the captured intensities. This birefringent intensity variation is depicted for an example cylindrical fiber with a fiber orientation angle θ_{fiber} of 90° (Fig. 1b). The bimodal intensity response is periodic over a 180° range and has a *global maximum* where $\theta_{polarizer}=\theta_{fiber}$ with a corresponding offset *local maximum* when $\theta_{polarizer}=\theta_{fiber}\pm 90°$. The global and local maxima occur when the polarizer transmission axis is parallel to and perpendicular to the fiber orientation angle θ_{fiber}, respectively. Quantitatively, the birefringent reflected intensity I_{out} of a group of collagen fibers (Fig. 1b) can be described by the following 3-term Fourier cosine series:

$$\frac{I_{out}}{\tau_{sys}} = a_0 + a_2\left[2\left(\theta_{fiber} - \theta_{polarizer}\right)\right] + a_4\left[4\left(\theta_{fiber} - \theta_{polarizer}\right)\right], \tag{1}$$

where τ_{sys} is a bulk systemic coefficient encompassing non-birefringent intensity modifiers, such as the aperture of the camera, and a_0, a_2, and a_4 are the three Fourier coefficients. Specifically, a_0 describes the mean reflected light intensity from the sample, whereas a_2 and a_4 represent the *optical anisotropies* arising from the sample's birefringence. Equation (1), derived on the basis of a standard Stokes/Mueller formalism [33, 50, 51], with more details presented in Appendix A, represents the reflected intensity of a single fiber with orientation θ_{fiber}, or a group of fibers with a mean angle θ_{fiber}, as a function of $\theta_{polarizer}$.

For complex clusters of collagen fibers with varied in-plane orientations, the magnitudes of the optical anisotropies provide a means of examining the local dispersion of the collagen fibers, which is expressed in the degree of optical anisotropy (DOA), i.e.,

$$DOA = \frac{a_2 + a_4}{a_0 + a_2 + a_4}. \tag{2}$$

Although the DOA metric is not a perfect indicator of the dispersion of collagen fibers, as the observed optical anisotropy can be influenced by factors including the tortuosity of the constituent fibers and non-lamellar fiber arrangement [33], the DOA could still provide valuable comparative information about the dispersion of collagen fibers throughout a sample. The DOA may also allow for important relative comparisons of the collagen microstructures within a tissue sample subjected to various mechanical loading conditions (cf. Section 3).

Remark 1: Equations (1) and (2) underlie the fundamental theory of birefringent collagen scattering, which relates the birefringent optical response of a collagenous tissue to the mean fiber orientation θ_{fiber} and the approximate fiber dispersion by means of DOA. In the pSFDI implementation (cf.

Section 2.3), these relationships are used to extract the spatial collagen structural information from a sample's optical response.

2.2 Spatial frequency domain imaging (SFDI) theory

pSFDI employs the spatial frequency domain imaging (SFDI) theory to control the *effective imaging depth* in the collagen microstructural quantifications. Specifically, SFDI relates the effective penetration depth $\delta_{eff,AC}$ of the measurements to the *spatial frequency* f_x of the projected light pattern by the following approximation

$$\delta_{eff,AC} \approx \frac{1}{2\pi f_x}. \tag{3}$$

Remark 2: By judiciously regulating the incident light's spatial frequency, pSFDI can produce spatial maps of the tissue's optical properties encoding only information shallower than a desired effective imaging depth, according to Eq. (3) (see Figure B1), where tissue depth is defined as the distance from the light-tissue interface into the sample medium. This capability is possible because the amplitude modulation of the AC intensity signal within the sample depends upon the incident spatial frequency, where higher spatial frequency signals diffuse at shallower imaging depths, and conversely, lower spatial frequency signals will retain their amplitudes further into the tissue [52] (cf. Fig. B1).

Remark 3: The depth-controlled images generated from SFDI are known as the *AC images*, as they capture the *spatially alternating* reflected intensities. In the SFDI image demodulation process, as discussed extensively in literature, these depth-controlled AC images are generated together with full-optical-thickness images, denoted as the *DC images*, since they represent signals that are independent of spatial modulations in the reflected light patterns. For this reason, results derived from the DC image signals are independent of the incident spatial frequency f_x. For interested readers, we provide a detailed analysis of the relation (Eq. (3)) between the spatial frequency and the imaging penetration depth, as well as a description of the image demodulation process and a discussion of the DC and AC imaging depth formulae in Appendix B.

2.3 Polarized spatial frequency domain imaging system

The pSFDI imaging technique combines the ability of co-polarized imaging to quantify the birefringent fiber structures with the depth-discrimination capabilities of SFDI. A pSFDI system (Fig. 2) was developed in our lab, which utilizes an LED-driven, micromirror-based pattern projection system (Texas Instruments, Dallas, TX) with a projection wavelength of 490 nm (cyan) and a 5 Megapixel CCD camera (Basler, Germany) with lens of *f/1.9* and an exposure time of 50 ms. For controlled rotational polarization, our pSFDI system employed a nanoparticle linear polarizer with a diameter of 25 mm mounted into a rotational servo motor with a 0.1° resolution (Thorlabs, Newton, NJ). These components were attached

firmly to a vertical breadboard using a combination of purpose-built 3D-printed components and standard optics mounting hardware (Fig. 2). For imaging of the load-dependent collagen microstructures in soft collagenous tissues (cf. Sections 2.4.2 and 2.4.3), we further integrated this polarized spatial frequency domain imaging system with a commercial biaxial mechanical testing system (BioTester, CellScale, Ontario, Canada) to form a novel opto-mechanical instrument (Fig. 2).

During testing, the projection-system projected three phase-shifted images sequentially, through a polarizer at angle $\theta_{polarizer}$, onto a tissue sample. For each projected image, the reflected light from the sample passed back through the same polarizer and was captured by the CCD camera. This projection-capture sequence was repeated at each of the 37 discrete polarization increments (5° increments from 0° to 180°). The coordination of the image projection, image capture and polarizer rotation were accomplished through a custom LabView program (National Instruments, Austin, TX).

After pSFDI testing, the phase-shifted images were first smoothed via convolution with a normalized 5×5 uniform kernel and were then combined at each pixel and polarization state according to the convention from the SFDI theory (cf. Appendix B for more details). *At each pixel* in the resultant DC and AC images, the following analysis processes were performed:

- **i.** fit the intensity vs. $\theta_{polarizer}$ data by using the 1D moving least-squares (MLS) function [53];
- **ii.** extract the local θ_{fiber} from the MLS fit as the polarizer angle where the model intensity was maximized, using the NumPy argmax() function;
- **iii.** compute the cosine terms in Eq. (1), utilizing the extracted local θ_{fiber};
- **iv.** use the calculated cosine terms to perform linear least-squares curve fitting on the intensity with respect to $\theta_{polarizer}$ to determine the three coefficients (a_0, a_2, a_4) from Eq. (1);
- **v.** apply coefficients (a_0, a_2, a_4) to Eq. (2) to compute the local (pixel-wise) DOA.

The above algorithm was found to be more computationally effective for extracting the structural metrics (θ_{fiber} and DOA) than an alternative nonlinear curve fitting process, which requires a judiciously-chosen initial guess. In addition to these steps, the effective imaging penetration depth of structural metrics extracted from the AC intensity data was computed using Eq. (3). All the above data analyses were implemented via in-house Python and MATLAB (MathWorks, Natick, NA) programs.

2.4 Imaging of the load-dependent collagen microstructural architecture for representative soft collagenous tissues

All tissues used in the following studies were obtained from a USDA-certified abattoir (Country Home Meat Co., Edmond, OK). The tissues were frozen for storage purposes and thawed prior to testing and sample selection, based on prior studies which showed the freezing process has minimal effects on the tissue microstructures and the mechanics [54–56].

2.4.1 Verification testing for the developed pSFDI system – bovine tendon tissues—

First, to assess the microstructural predictions by the developed pSFDI system, verification imaging tests were performed on bovine tendon samples. In the interior region of tendon, collagen fibers exhibit a strong preferential alignment along the longitudinal tendon axis [49, 57, 58]. To evaluate the efficacy of the system's microstructural predictions, the quantified collagen fiber orientations of tendon samples were compared to the expected preferential orientation *a priori*. In brief, three thin tissue samples were excised from the central region of bovine tendons, with care taken to exclude the synovial sheath membrane enclosing the tendon. The samples were placed at varied planar orientations (Fig. 3a), sandwiched between two microscope slides in a 3D-printed container, and mounted to the pSFDI system. Tissue samples were imaged with a spatial frequency of f_x=0.20 mm^{-1}. Because this group focused on the verification of the fiber orientation predictions of our developed pSFDI system, we considered only the DC, or full-depth, image results from this study.

2.4.2 Quantification of load-dependent CFA changes – bovine tendon tissues—

Next, displacement-controlled uniaxial stretching tests were performed to examine the load-dependent changes in the collagen fiber microstructures of the bovine tendon tissue. Specifically, a strip of tissue (thickness of 1.25 mm, width of 15 mm, length of 40 mm) was sectioned from the central region of a bovine tendon, such that the strip length direction was aligned with the native tendon axis. The tendon sample was then mounted to the biaxial mechanical testing system via the CellScale clamp mounting fixture (Fig. 2) and subjected to various longitudinal strains (0%, 1%, 2% and 3%) along the tendon tissue's length direction (Fig. 4a). At each strain state, the collagen fiber orientation and the DOA within the sample were quantified using the developed pSFDI system with a spatial frequency of f_x=0.20 mm^{-1}. Sample hydration was maintained by soaking the sample in phosphate-buffered saline (PBS) solution between the imaging tests.

2.4.3 Quantifications of load-dependent CFA changes – porcine mitral valve anterior leaflet (MVAL) tissues—

Heart valve leaflets, such as the mitral valve anterior leaflet (MVAL), exhibit spatially-varied CFAs with complex layer-dependent microstructures [59–62]. Two studies examined the complex MVAL tissue microstructures: *Study A*, to examine how the collagen fiber microstructures changed in response to varied biaxial mechanical loads, and *Study B*, to assess the differences in the load-varied tissue CFA at distinct measurement depths.

In each of these two studies, the entire anterior leaflet tissue samples were excised from the porcine mitral heart valve, and three thickness measurements via a digital caliper (Westward 1AAU4 – 0.01 mm resolution) were taken across the domain of the tissue with the average thickness reported. Then, the leaflet was mounted to the BioTester using the CellScale BioRakes fixture to create an effective testing region of 10×10 mm (Fig. 5a). The MVAL tissue sample's circumferential and radial directions were aligned with the x- and y-axes of the tester, respectively, during mounting. The tissues were then immersed in a PBS solution at 37 °C for the duration of mechanical testing to emulate the valve's physiological conditions. Prior to applying the mechanical testing protocols, the tissue samples were

preconditioned to restore their *in vivo* functional state using a standard force-controlled preconditioning protocol with a targeted maximum force of 1N applied in both the circumferential and radial directions [63, 64]. The targeted loading of 1N was determined based on an assumed physiological membrane tension of 100 N/m [65–67] and a 10 mm effective edge length.

In *Study A,* an MVAL tissue sample with a thickness of 0.75 mm was examined. After the above-mentioned preconditioning step, the tissue sample was subjected to various biaxial loads: F_C:F_R=1000 mN:1000 mN, F_C:F_R=1000 mN:250 mN, and F_C:F_R=250 mN:1000 mN, where F_C and F_R are the forces applied in the circumferential and radial directions, respectively. A spatial frequency of f_x=0.27 mm^{-1} was adopted for all tests in *Study A* with only the DC, or *full-depth*, image results reported.

In *Study B*, another MVAL tissue sample with a thickness of 0.87 mm was subjected to mechanical preconditioning and then examined with spatial frequencies of 0.71 mm^{-1}, 0.42 mm^{-1}, 0.24 mm^{-1}, and 0.20 mm^{-1}, which *correspond to the AC imaging depths of 225 μm, 375 μm, 650 μm, and 800 μm, respectively, based on* Eq. (3). The MVAL tissue sample was then loaded with F_C:F_R=1000 mN:1000 mN, and the pSFDI imaging was repeated using the same set of spatial frequencies mentioned above. Both the AC and DC image results were compiled and reported from this study.

Remark 4: The procedures for *Study A* were repeated with the MVAL tissue sample used in *Study B*, for a brief examination of the cross-leaflet consistency in the predictions of the collagen fiber microstructural architectures (Fig. 2). The results of this repeated testing are included in Appendix C (Figs. C1–C2 and Table C1).

3 Results

3.1 Collagen microstructural imaging for bovine tendon tissues – unloaded state

The predictions of the collagen fiber orientation θ_{fiber} by our developed pSFDI system for three bovine tendon samples are presented in Figure 3. Three key results from this imaging study are summarized as follows. First, by extracting the peak of the modelled MLS intensity from representative pixels (red circles in Fig. 3a), the single-pixel predictions of the collagen fiber orientation associated with the above three tendon tissue samples were determined and reported as 122.7°, 55.1°, and 20.4°, respectively (Fig. 3a). Second, the 3-term Fourier cosine series in Eq. (1) was able to accurately model the local pixel-by-pixel birefringent reflected intensities of the collagenous tissues at the three selected pixel points (R^2≥0.994, Fig. 3b). Finally, the spatial predictions of the fiber orientation θ_{fiber} (Fig. 3c) are consistent with the longitudinal axis of the tendon throughout the tendon tissue domain, with distributions falling in the range of 119.3°±2.5°, 58.8°±2.8°, and 25.6°±5.0°, respectively (median±0.5*IQR; IQR=Q_3-Q_1 refers to the interquartile range), which closely match the respective longitudinal tendon axes of the three bovine tendon tissue samples as oriented at ~120°, ~60°, and ~25°. These collagen microstructural imaging results considering tissues at the unloaded state provided a qualitative and quantitative verification of the pSFDI system. The result of this study supported our investigations into the effects of external mechanical

loading on the tendon tissue's collagen fiber microstructures, which will be discussed in the next subsections.

3.2 Collagen microstructural imaging for bovine tendon tissues – loaded states

Another strip of bovine tendon tissue—with a thickness of 1.25 mm, a width of 15 mm, and a length of 40 mm—was prepared, mounted onto the biaxial tester such that the collagen fibers of the tissue sample were oriented at approximately 52°, and uniaxially loaded to 0%, 1%, 2%, and 3% strain ε (cf. results of 0% and 3% longitudinal strains in Fig. 4a,b). The predicted fiber orientation θ_{fiber} throughout the entire tissue domain were, in general, unaffected by the applied uniaxial loading in the sample axial direction (longitudinal strain of 0% versus 3%, Fig. 4b). Unlike the fiber orientation predictions, the predicted DOAs increased heterogeneously across the tissue domain in response to the longitudinal strain (0% versus 3%, Fig. 4c). By further investigating the optical signal averaged over a bulk region of the tendon tissue (cf. the inlet of Fig. 4d), a marked increase in the magnitude of the optical birefringence in response to the applied uniaxial loading was observed. These increases in the optical anisotropy were captured by the corresponding increase in the DOAs. For example, the DOA values averaged over the region shown in red (Fig. 4d) were reported as mean±SD: 0.149±0.039, 0.169±0.043, 0.188±0.051, and 0.198±0.060 for the 0%, 1%, 2%, and 3% longitudinal strains, respectively. Moreover, the DOA distributions for the tendon tissue at each loading state are presented in the Supplementary Material section (Fig. S1), together with the one-way ANOVA revealing the statistically significant ($p<0.001$) differences in local DOA distributions between any two loading states. The significant and expected increase in the quantified DOAs with the increased tissue loading supports its use to represent the fiber straightening, local decreases in the fiber dispersion, and the overall fiber recruitment of soft collagenous tissues. For example, as tissues are loaded, collagen fiber groups exhibit a more uniform alignment in the direction(s) of the applied loading [44, 46, 68]. Our integrated instrument was able to quantify this important load-dependent microstructural characteristic through the DOA metric.

3.3 Collagen microstructural imaging for mitral valve leaflet tissues

The integrated pSFDI-biaxial opto-mechanical instrument was employed to capture the load-dependent changes in the collagen fiber microstructures of MVAL tissue samples subjected to various biaxial loads. The CFA for each MVAL sample at each loading state is illustrated through three graphical representations: (i) colormaps of the pixel-wise DOA over the tissue at each loading state (Fig. 5 and Fig. C1), (ii) superimposed streamlines showing the spatially-heterogeneous preferred collagen fiber orientation θ_{fiber} (Fig. 5 and Fig. C1), and (iii) histograms of the distributions for both the fiber orientation θ_{fiber} and DOA over the tissue domain (Fig. 6 and Fig. C2). The results, which are *the first of their kind* with the MVAL tissue, indicate that the collagen fiber architecture of the MVAL tissue samples is both *spatially non-homogeneous* and *highly load-dependent* (Figs. 5–6 and Figs. C1–C2). Specifically, at the unloaded state, the fibers were generally aligned in an extended U-shape —tracing an arc from the left commissure, toward the coaptation point, and back to the right commissure (Figs. 5b and C1a). This microstructure has been well-catalogued in the heart valve leaflets [23, 44, 69]. Moreover, the predicted DOAs at the unloaded state were relatively uniform, falling into a range of 0.02–0.08 throughout the tissue domain (Figs. 5b,

6c, C1a, and C2b). Drastic and spatially-varied changes in both the predicted fiber orientations and DOA were observed when the MVAL tissue samples were subjected to various biaxial loading protocols (cf. Fig. 5c–e for the first MVAL tissue sample and Fig. C1b–d for the second MVAL tissue sample).

Remark 5: Although the fiber orientations over the two representative MVAL tissue specimens were presented graphically via the streamlines in Figures 5 and C1, the θ_{fiber} measurements were obtained at each individual pixel over the tissue domain, similar to those presented in Figure 7(b). The streamline representation was adopted here only to visually demonstrate the load-dependent fiber orientation changes concurrently with the local DOA changes.

3.3.1 Examinations of the spatially-varied predicted fiber orientations and DOAs—

The distributions of the predicted fiber orientation θ_{fiber} for the MVAL tissue sample exhibited bimodal appearances, especially in the unloaded, equibiaxially-loaded, and radially-dominant loading states (Figs. 6b,c and C2a,b). Based on the previous studies suggesting the presence of multiple fiber groups in the heart valve leaflets [70] and the observed bimodal characteristic of the predicted CFAs, bimodal distributions were used to quantify the distributions of θ_{fiber} at each loading state.

To evaluate the quantified fiber orientations, a bimodal π-periodic von Mises distribution $\hat{f}(\theta_{\text{fiber}})$ was employed, which takes on the form

$$\begin{aligned}\hat{f}\left(\theta_{fiber}|\mu_1,\kappa_1,\mu_2,\kappa_2,w\right) &= wg^{von-Mises}\left(\theta_{fiber}|\mu_1,\kappa_1\right)\\ &+(1-w)g^{von-Mises}\left(\theta_{fiber}|\mu_2,\kappa_2\right),\end{aligned} \tag{4}$$

and

$$g^{von-Mises}(\theta|\mu,\kappa)=\frac{1}{\pi I_0(\kappa)}\exp[\kappa\cos[2(\theta-\mu)]], \tag{5}$$

where (μ_1,κ_1) and (μ_2,κ_2) are the parameters associated with the *first* and *second* von Mises distribution groups, respectively (cf. Figs. 6b and C2a), I_0 is the Bessel function of the first kind of order 0, $w\in[0,1]$ is the mixing parameter describing the relative magnitudes of the two distribution groups. More specifically, the μ_1, μ_2 parameters denote the center of the *first* and *second* fiber distribution groups, respectively, similar to the means of a corresponding bimodal normal distribution, and $\kappa\in[0,1]$ denotes the concentration parameter of these fiber distribution groups representing an inverse measure of dispersion. Note that the concentration parameter κ can be considered analogous to $1/\sigma^2$, where σ is the standard deviation of a corresponding normal distribution [71].

Remark 6: It should be noted that the assumption of bimodal microstructural distributions was made to allow *quantitative* evaluations of the θ_{fiber} distributions of the MVAL tissue samples, as well as their dependence on the applied biaxial loads. While other models, such as a unimodal von Mises distribution, may represent the θ_{fiber} distribution at specific loading

states, the chosen bimodal model is able to represent the fiber structure at *each* loading state (as shown in Figures 6 and C2) and thus suffices for our demonstrative purposes.

Remark 7: To further investigate the spatial variance in the distributions of the quantified θ_{fiber} and DOA at each loading state, the MVAL specimen domain was discretized into 4×4 grids (Fig. S2) and the CFA resutls were analyzed individually. The results of this regional analysis are shown in the Supplementary Material section (Figs. S3 and S4 for MVAL tissue samples #1 and #2, respectively). These regional distributions shed light on the spatial variations in the load-dependent fiber orientation θ_{fiber} and DOA within the MVAL tissue specimen.

Remark 8: Although the global histograms showed a bimodal distribution (Figs. 6b and C2a), the distribution of the local results (see Figs. S3 and S4 in the Supplementary material) was rather unimodal, indicating a high non-homogeneity of the MVAL tissue. Thus, the presented parameters of the bimodal distributions in Eqs. (4)–(5) are not directly suitable for local applications, such as finite element modeling as described in [10, 72, 73], but instead the quantified "pixel-wise" fiber direction and fiber dispersion should be used.

3.3.2 Changes in the fiber orientation and DOA distributions of the MVAL tissue samples under biaxial mechanical loading—

The fitting parameters, the coefficient of determination (R^2) for each model fit, and the tissue stretches are presented for each loading ratio in Table 2 for the first MVAL sample, and in Table C1 for the second MVAL sample. For both tissues, the distributions changed with the applied loading. In this section we discuss these changes with respect to the distinct loading ratios. Note that these results are specific to the two (n=2) representative MVAL tissues examined in this study, and are not intended to describe population-based microstructural features.

Changes in the CFAs of the MVAL from the unloaded state to the equibiaxial loading state: Although no consistent changes in the θ_{fiber} group centers/means (μ_1 and μ_2) were observed from the unloaded state to the equibiaxial loading state (F_C:F_R=1000 mN:1000 mN) across the two MVAL tissue samples we examined, consistent changes in the fiber distribution group concentrations (κ_1 and κ_2) were observed. Specifically, κ_1 *decreased* with the applied equibiaxial loading: for the first MVAL sample $\kappa_1=0.347\times10^{-3}$ (unloaded) and $\kappa_1=0.148\times10^{-3}$ (equibiaxial loading) (Table 2), whereas for the second MVAL sample $\kappa_1=0.725\times10^{-3}$ (unloaded) and $\kappa_1=0.122\times10^{-3}$ (equibiaxial loading) (Table C1). In the meantime, κ_2 *increased* with the applied equibiaxial load: for the first MVAL sample $\kappa_2=2.42\times10^{-3}$ (unloaded) and $\kappa_2=2.84\times10^{-3}$ (equibiaxial loading) (Table 2), whereas for the second MVAL sample $\kappa_2=1.03\times10^{-3}$ (unloaded) and $\kappa_2=8.42\times10^{-3}$ (equibiaxial loading) (Table C1). These quantitative concentration changes reflect the *qualitative* changes, as observed in Figures 6b and C2a, where the spread of the first fiber group distribution increased, and the spread of the second fiber group decreased from the unloaded state to the equibiaxial loading state. Concurrently with the investigation of the CFA, the mechanical

deformations of the tissue were determined by the BioTester. Under the equibiaxial loading, the radial stretch λ_{Rad} of MVAL Specimen #1 was 1.27, whereas the circumferential stretch λ_{Circ} was only 1.17 (Table 2). Similarly, for the second representative MVAL tissue specimen, the radial stretch λ_{Rad} and the circumferential stretch λ_{Circ} were 1.34 and 1.19, respectively (Table C1), revealing the anisotropic tissue mechanics and higher circumferential stiffness as observed for heart valve leaflets in literature [74–76].

Changes in the CFAs of the MVAL from the unloaded state to the radially-dominant loading: When the radially-dominant loading protocol (F_C:F_R=250 mN:1000 mN) was applied, the first fiber distribution group exhibited consistent changes across the two MVAL speciments. Specifically, μ_1 moved towards the tissue's radial direction (θ=90°) in accordance with the radially-concentrated loading: for the first MVAL tissue sample, μ_1 shifted from 49.1° (unloaded) to 78.1° (under radially-dominant loading) (Table 2), whereas μ_1 shifted from 72.8° (unloaded) to 89.8° (under F_C:F_R=250 mN:1000 mN) in the second MVAL tissue sample (Table C1). Similarly, κ_1 increased from 0.347×10^{-3} (unloaded) to 0.917×10^{-3} (under radially-dominant loading) (Table 2) for the first MVAL tissue sample, whereas for the second MVAL sample, κ_1=0.725×10^{-3} (unloaded) increased to κ_1=1.139×10^{-3} (under radially-dominant loading) (Table C1). Unlike the first fiber group, the changes in both the mean and concentration of the second fiber group between the unloaded and radially-dominant loading states were observed to be minimal from the two MVAL specimens examined. Comparing the quantified DOA between the unloaded and the radially-dominant loading states, the mean DOA increased from 0.043 to 0.077 in MVAL Specimen #1 (Table 2), and similarly from 0.034 to 0.061 in MVAL Specimen #2 (**Table C2**).

Changes in the CFAs of the MVAL from the unloaded state to the circumferentially-dominant loading: The circumferentially-dominant loading (F_C:F_R=1000 mN:250 mN) caused changes in the second fiber distribution group. Specifically, μ_2 moved towards the circumferential axis under this circumferential direction (θ=180°) favored loading: μ_2=151.1° (unloaded) and μ_2=165.3° (under circumferentially-dominant loading) for the first MVAL tissue sample (Table 2), whereas the observed change was less noticeable for the second MVAL tissue sample, i.e., μ_2=166.4° (unloaded) and μ_2=167.0° (under F_C:F_R=1000 mN:250 mN) (Table C1). Similarly, κ_2 increased with the applied circumferentially-dominant load, indicating the reduced variance of the second fiber distribution group: for the first MVAL tissue sample, κ_2=2.42×10^{-3} (unloaded) and κ_2=4.32×10^{-3} (under circumferentially-dominant loading) (Table 2), whereas for the second MVAL κ_2=1.03×10^{-3} (unloaded) and κ_2=5.46×10^{-3} (under circumferentially-dominant loading) for the second MVAL tissue sample (Table C1). Moreover, the mean DOA increased from 0.043 (unloaded) to 0.086 (circumferentially-dominant loading) for MVAL Specimen #1, and similarly from 0.034 to 0.082 for the second MVAL specimen. For both MVAL tissue specimens, the mean DOA value under the circumferentially-dominant loading regime was comparable to that under the equibiaxial loading (i.e., 0.075 and 0.089 for MVAL Specimens #1 and #2, respectively), which were both *higher* than the mean DOA under the radially-dominant loading (0.077 and 0.061 for MVAL Specimens #1 and #2, respectively).

3.4 Quantification of the transmural CFAs for the MVAL tissue

The microstructure of an MVAL tissue sample was analyzed at various depths according to Eq. (3). To provide further insight into these results, a cross-sectional histological view of a representative MVAL layered microstructure (using the Masson's trichrome stain) is shown in Figure 7a, where collagen fibers were stained in blue and each of the four morphologically-distinct layers was labeled with its respective thickness [77]. In the present work, an MVAL tissue specimen with a thickness of 0.87 mm was examined from the atrialis-side considering various imaging depths (Fig. 7b). The unloaded tissue was first imaged using the pSFDI system at each penetration depth from 225 μm to 800 μm (Fig. 7b), then subjected to an equibiaxial load of F_C:F_R=1000 mN:1000 mN and imaged again with the same pSFDI protocols (Fig. 7c). At the unloaded state, the fiber orientations showed a substantial depth-variance. For example, the predicted fiber orientation changed from ~90° at the shallowest imaging depth (225 μm) to ~0° as the imaging depth increased (cf. black square in Fig. 7b). Similar depth-dependent variance in the fiber orientations were observed in the upper-central region of the unloaded test (cf. black circle in Fig. 7b), where the predominant fiber orientation changed from ~160° to a mixture of ~0° and ~70° fiber orientations as the imaging depth increased. To further visualize the regional differences in the transmural (depth-dependent) collagen fiber microstructures, each MVAL tissue domain outlined in Figure 7c was further subdivided into 2×3 grids, and the distributions of θ_{fiber} and DOA were plotted within each subregion (Figs. S5–S6 and Figs. S7–S8). These results indicate that the spatial organization of collagen fibers may be different in the uppermost atrialis layer from the inferior layers for the *unloaded* MVAL tissue (Fig. 7c, Fig. S5, and Fig. S7). In contrast, these depth-dependent discrepancies were indiscernable when the MVAL tissue was subjected to the *equibiaxial loading* (Fig. 7c, Fig. S6, and Fig. S8). Specifically, the quantified fiber orientations in the loaded tissue were nearly independent of the pSFDI-imaging depth over the spatial frequency range examined in this study (f_x=0.20–0.71 mm^{-1}). Our novel findings from the representative MVAL tissue specimen suggests that, while fiber orientations may vary across the tissue layers at the unloaded state, the collagen fiber orientations under equibiaxial loading may remain relatively uniform throughout the tissue's transmural (thickness) direction (Fig. 7c and Figs. S5–S6).

4 Discussion

4.1 General findings

4.1.1 Opto-mechanical testing on tendon tissues—This study has demonstrated the capability of an integrated biaxial pSFDI instrument to quantify the collagen microstructures of soft collagenous tissues under various mechanical loading conditions. Because pSFDI is a recently-established technique, the first goal of this study was to provide verification of the developed pSFDI system's capabilities. The performance of our pSFDI system was assessed through imaging of three bovine tendon samples, each oriented with a different preferred fiber direction (Fig. 3). An existing theoretical framework [33, 78] was applied to the pSFDI results of the tendon samples, with the accuracy of the 3-term cosine Fourier fitting validated by the local goodness-of-fit (R^2≥0.994) of Eq. (1) to the acquired intensity data. The quality of this fitting supported the extraction of the local fiber orientation θ_{fiber} from the acquired pSFDI data. The θ_{fiber} predictions were also found to be

spatially consistent throughout the tissue's domain (Fig. 3c), further verifying our pSFDI-based predictions given the known spatial-consistency of tendon tissues [79].

To further examine the use of DOA to represent the local degree of fiber alignment, a single tendon tissue sample oriented at ~52° under various uniaxial loads was considered. As predicted, the axial loading resulted in an increase in the magnitude of the tissue's optical anisotropy (Fig. 4b), which correlated with the known extension and reorientation of collagen fibers in uniaxially-loaded tendon tissues [80]. The magnitude of such an optical anisotropy was captured in the DOA metric, which increased from 0.149±0.032, 0.169±0.037, 0.188±0.045, to 0.198±0.056 (mean±SD) for a bulk tendon tissue region (Fig. 4d) under 0%, 1%, 2%, and 3% longitudinal strains, respectively. This substantial change in the DOA was accompanied by the relatively minimal change in the fiber orientation, with an average fiber orientation $\theta_{fiber,avg}$ differing by only 1.1° between all the considered loading states. Owing to its correlation with the straightening, extension, and re-orientation of the collagen fibers, the DOA could be used as a relative measure of the local collagen fiber's degree of alignment. The DOA metric showed that the specific loading pattern used caused uneven changes in local collagen fiber DOA in the tendon sample, as evidenced by the observed bands of higher DOA values in the direction of the applied loading (Fig. 4c). Correspondingly, during testing it was observed that the loading caused transverse creases and wrinkling in the tendon tissue, where fiber bands under higher loading tended to rise above the other tissue regions. This non-uniformity in collagen fiber recruitment was captured by the pSFDI results (Fig. 4b,c) for the uniaxially-loaded tendon tissue. These important findings support the validity of our developed pSFDI system and its underlying theoretical framework—the use of Eqs. (1) and (2) to extract the collagen microstructural architecture, i.e., θ_{fiber} and DOA.

4.1.2 Imaging of the load-dependent collagen microstructure for representative MVAL tissue samples—

Our first study considering the MVAL tissues examined how the tissue's CFA changed when the tissue was subjected to varied biaxial loading conditions. Through pSFDI imaging, it was revealed that the collagen fiber orientation within the MVAL leaflet was spatially-varied under the unloaded state (Figs. 5b and C1b), and that the CFA changed heterogeneously throughout the tissue domain, depending upon the dominant direction of the applied biaxial loading (Figs. 5c–e and C1c–e). These observations regarding the *atrioventricular heart valve leaflet* were inconsistent with the results of previous assessments of the *semilunar heart valve* leaflets [45, 81]. Specifically, the prior studies used SALS techniques to examine the aortic and pulmonary valve leaflet tissues under pressure loading, finding that the loading caused approximately uniform changes in the local degree of alignment of the collagen fibers, but relatively minor changes in the local fiber orientations. The discrepancies between these existing results and the present study may arise from two potential sources: (i) the inherent differences in the microstructural composition between the semilunar valve (i.e., the aortic valve and pulmonary valve) leaflets and the mitral valve anterior leaflet (one of the atrioventricular heart valve leaflets); and (ii) the distinctions of the applied loading condition, i.e., pressure loading for the studies by Sacks *et al.* (1998) and Joyce *et al.* (2009) [45, 81] versus the controlled biaxial mechanical loading in the present study. Previous mechanical loading

studies have shown that the loading form can significantly impact the observed mechanical responses [82–84]. It is likely that different mechanical loading conditions may cause distinct load-driven microstructural changes, contributing to the discrepancy in the observed CFAs.

Additionally, under certain biaxial loading conditions, primarily the unloaded, the equibiaxial loading (F_C:F_R=1000 mN:1000 mN), and the radially-dominant loading (F_C:F_R=250 mN:1000 mN) states, it was found that most of the distributions of the quantified fiber orientation θ_{fiber} exhibited a bimodal characteristic (Figs. 6 and C2). The distribution of θ_{fiber} under each loading protocol was thus modeled via a bimodal von Mises distribution (cf. Section 3.3.1). The center μ_1 of the first fiber group varied between 0° and 90° for both MVAL tissue specimens in response to the applied loading. Specifically, μ_1 moved towards the tissue's radial direction (θ=90°) under radially-dominant loading (F_C:F_R=250 mN:1000 mN), and similarly towards the circumferential direction (θ=0° or 180°) under circumferentially-dominant loading (F_C:F_R=1000 mN:250 mN). In contrast, the center μ_2 of the second fiber group was found to be relatively consistent for both MVAL tissues examined, ranging between 151.1° and 167.0° under all the examined loading conditions. In other words, this second fiber distribution group represented fibers *consistently* oriented nearer the circumferential direction (θ=0°) than the radial direction (θ=90°), whereas the preferred tissue direction of the first group varied on the basis of the loading state. It was further observed that loading scenarios with the applied forces concentrated in the circumferential direction (F_C:F_R=1000 mN:1000 mN and F_C:F_R=1000 mN:250 mN) resulted in higher DOA values than the radially-dominant loading protocol (F_C:F_R=1000 mN: 250 mN) (Figs. 6c and C2b).

These results describe the load-dependent CFA changes across the heterogenous MVAL tissue samples (Figs. 5 and C1). To comprehensively investigate the spatial heterogeneity of the load-dependency, the MVAL tissue domain was subdivided into 4×4 regions (Figs. S2–S4). Through this further analysis, several load-dependent CFA trends were exhibited in different regions. For example, although the DOA values under the radially-dominant loading were *on average* lower than those under the circumferentially-dominant loading, they were higher under the radially-dominant loading in certain regions—*the top right of the MVAL Specimen #1* (Fig. S3d) *and the bottom left of MVAL specimen #2* (Fig. S4d). These intricate spatial differences may suggest re-evaluation of the common expectation that fibers in the heart valve leaflets are predominately oriented in the tissue's circumferential direction, and that biaxial loading imposes a relatively homogeneous strain state within the tissue. Similarly, these spatial distinctions in the load-dependent CFA's are not readily quantifiable at a wide field of view (e.g., 10×10 mm) by other existing collagen imaging systems, and affirm the uniqueness of our study.

Through the depth-modulation capability of the pSFDI system, our study showed that the collagen fiber orientations in the representative MVAL exhibited transmural variance at the unloaded case, compared to a nearly homogenous fiber orientation throughout the tissue depth when the MVAL tissue was subjected to equibiaxial mechanical loading. These novel results suggest that, while the microstructure of the MVAL exhibits a proclivity towards the circumferential direction, the collagen fibers are *neither consistently nor uniformly* aligned

in a single direction, especially with regard to the differences between the layers and the spatial differences (as further illustrated in Figs. S5–S6 and Figs. S7–S8). These findings are supported by a recent biaxial mechanical testing study which found distinct mechanical properties in each atrioventricular valve leaflet layer [59]. Through this SFDI-driven approach, the spatial and transmural distribution of the load-dependent collagen fiber orientations and DOA of the MVAL tissue were investigated for the first time. The utility of the integrated biaxial pSFDI opto-mechanical instrument is evinced by such broad and novel investigations. Studies employing similar techniques may provide comparable quantitative measures of transmural variance in the collagen fiber architecture for soft collagenous tissues under arbitrary mechanical loading.

4.2 Relationship between the CFA and tissue mechanics in the MVAL

Our study, *which is the first of its kind* with the MVAL tissue, revealed the complexity of load-dependence in the microstructure of the MVAL tissue samples. These quantified microstructural attributes can shed light on many of the phenomena observed in mechanical studies on the MV leaflets, such as the material anisotropy, nonlinearity, and the observed spatial variations [85–87]. Our study also revealed that, although the collagen fibers in the MVAL are not perfectly oriented in the circumferential direction, the fibers demonstrate a predominant circumferential orientation even under preferential loading in the radial direction (Figs. 5d and C1c). This circumferential tendency corresponds to the higher circumferential stiffness and material anisotropy in the mechanical response of the heart valve leaflets (cf. the tissue stretch values in Table 2 and Table C1). Moreover, in terms of the spatial differences in tissue microstructures, our study demonstrated that the microstructures of the MVAL tissue sample were generally spatially heterogenous regardless of the applied loads (Figs. 5 and C1). The observed microstructural heterogeneity in the MVAL (Figs. S3–S4, Figs. S5–S6, and Figs. S7–S8) echoes the previous findings of the differences in the *mechanical properties* across different MVAL regions [85]. In addition to the material anisotropy and the regional variance, ongoing studies in our lab are using this integrated opto-mechanical instrument to examine the microstructural basis for the nonlinear mechanical response of the heart valve leaflets. Our preliminary results from our pilot study suggest that after a large amount of deformation and fiber realignment, indicated by the toe-region of the stress-strain curve, the CFA reaches a “terminal” point and will remain relatively unchanged upon further loading. This cessation of the microstructural change corresponds to a rapid stiffening in the tissue mechanics, thus enforcing the observed nonlinear mechanical curves. Thus, quantifying the load-dependent microstructure in membranous, collagenous tissues like the MVAL can allow explanation of the tissue mechanics from a microstructural basis. This deeper comprehension of the microstructure behind the tissue’s mechanical properties will be essential for improving the understanding of the diseased tissue states and for enriching computational models of the heart valve function [73, 88].

4.3 Study limitations and future work

4.3.1 Limitations of the existing integrated opto-mechanical instrument—

Despite the general accuracy of tendon tissue microstructural predictions, some local incorrect predictions existed. These mispredictions may be attributed primarily to the rough

sample surfaces rather than any systemic prediction biases. For example, during one of the tendon imaging experiments (with results depicted in the middle sample of Figure 3c), it was observed that the tissue was not completely flush against the microscope slides, especially in the right region of the tissue. The resulting non-smooth surface caused specular reflections, potentially leading to the incorrect fiber predictions. The systemic preference for a smooth sample surface was manifest further in the uniaxial testing on bovine tendon, where striations of mis-predictions of ~140° along the direction of the applied force were possibly caused by heterogeneous loading along the tissue width (Fig. 4b and Fig. S1). In addition, it was observed that loading caused collagen fiber bundles to be nonuniformly recruited, and thus form an uneven surface geometry, further contributing to the inaccuracies. This observation was supported by the DOA predictions for the loaded tissue, which show substantial spatial differences in fiber recruitment (Fig. 4c).

The surface effects found in the tendon analysis did not persist into the study of the MVAL microstructure due to the smooth leaflet surface and the PBS bath. However, because the MVAL tissues were kept hydrated in a solution bath during testing, we observed minor pointwise irregularities in the MVAL predictions due to impurities drifting on the surface of the PBS solution. We also observed some specular reflections from the surface of the PBS, but these “bright spots” were outside of the tissue domain (Fig. 5a). This issue could be mitigated via minor adjustments of the incidence angle of the pSFDI system with respect to the bath surface. Another experimental limitation was the use of the BioRake-based separation distances to determine the tissue stretches. In biaxial mechanical testing experiments, fiducial markers are typically placed on the tissue sample and tracked to compute the strains experienced by the tissue [64, 89, 90]. Due to optical interference, fiducial markers were not applied to the MVAL samples in this study, and we were thus unable to quantify the more accurate strain field of the tissue. The presented tissue stretch values may still serve as a good approximation to the tissue strain state. If a more accurate strain field was needed, finite element modeling, such as the one used in [91], could be applied with local anisotropic constitutive models based on the measured results. Finally, caliper-based thickness measurements presented in this study depend on the amount of force applied during the measurement, which may not be as accurate as other non-contact measurement techniques, such as the optical coherence tomography and a video-extensometer.

In the spatial frequency study (*Study B*), some banding appeared in the θ_{fiber} predictions of the unloaded tissue at the higher spatial frequencies (Fig. 7b). Since one of the purposes of demodulating the 3 phase-shifted initial images into the AC image is to ensure a uniform illumination, no indication of the projection pattern should appear in the resultant images. These bands did not appear at lower spatial frequencies, nor in the loaded tissue predictions (Fig. 7c). While our captured intensities encode predominantly information from the sample, a small amount of light that was reflected from the surface of the polarizer and captured by the camera. For larger spatial frequencies and more reflective samples, this minor reflection was negated by the signal from the tissue. Nevertheless, at high spatial frequencies and for samples with relatively weak birefringence signals, the reflected light from the polarizer may have caused the non-sinusoidal, skewed intensities in the phase-shifted images, leading to banding in the AC combined images. These minor errors could be remedied by systemic

normalizations and improved calibrations, like those described in the recent study by Goth *et al.* (2019) [35], or by restricting the incident spatial frequency to a given range. Despite the appearance of these bands, our system was able to capture the transmural changes to the microstructure that accompanied the loading in the representative MVAL tissue specimen.

4.3.2 Future improvements to the integrated biaxial pSFDI instrument—Like other emerging techniques, the pSFDI modality will presumably see a variety of improvements in the coming years. Recently, one such contribution came from Goth *et al.* (2019) [35], who developed a model to directly and quantitively relate the optical birefringence captured by the pSFDI system to the local dispersion of the collagen fibers via Monte Carlo simulations of light transport in the tissue media. Similar modeling approaches may lead to more accurate depth-modulated imaging and subsequently to a more precise characterization of layer-specific microstructures in soft collagenous tissues. Another improvement to the pSFDI modality may emerge from hardware advances, leading to increases in the imaging speed. Fundamentally, there should not be limitations on the pSFDI from sub-second acquisition time; the difficulty arises from the electrical and mechanical implementations of such a rapid imaging system. Despite this difficulty, a sub-second acquisition time would allow analyses of multiple mechanical and microstructural properties of soft collagenous tissues, including local fiber affine behaviors and CFA changes under stress relaxation testing. Furthermore, achievement of sub-second imaging speeds for the pSFDI system could allow quantification of changes to heart tissue microstructures at deformation rates approaching those experienced *in vivo* [44, 74].

4.3.3 Future investigations on tissue's microstructure—The integrated biaxial pSFDI instrument was able to monitor the changes in the local fiber networks in response to varied biaxial mechanical loads. This novel capability is a powerful tool for providing new insight into the tissue's fiber microstructures. Subsequent studies may be warranted to analyze: (i) the previously-impenetrable mechanical phenomena from a microstructural standpoint, such as the preconditioning effect, the stress-relaxation effect, and the nonlinearity in the collagenous tissue's mechanical responses; (ii) the transmural differences in the collagen fiber architecture kinematics in layered tissues, through the SFDI technique; and (iii) the load-dependent microstructures in a variety of planar collagenous tissues. For example, to the best of the authors' knowledge, no existing studies have quantified the microstructures of the tricuspid valve leaflets, with scholarly attention traditionally paid to the aortic, mitral, and pulmonary valve leaflets despite the prevalence and detriment of tricuspid valve diseases [47, 63, 66, 85, 92, 93]. Future studies could include opto-mechanical characterizations of the tricuspid valve leaflet tissues (with a statistically-meaningful sample size) or other non-valvular soft collagenous tissues, such as skin, arteries or the gastrointestinal wall, to build a population-based understanding of the features of the tissue-specific collagen microstructures as a function of the mechanical loads. Through quantifications of the microstructural changes of tissues under loading via integrated pSFDI imaging, an improved understanding of the tissues' physiological behaviors could be gained.

4.3.4 Applications of CFA quantifications towards medical practice—There are several potential applications of the load-dependent microstructural quantifications derived

from pSFDI towards medical practice. Firstly, the system described herein and similar devices have direct applications towards evaluating the load-dependent properties of experimental replacement of biomedical membrane materials, especially as they relate to the properties of the native biological tissues. These investigations would allow improved understanding and prediction of the material behavior *in vivo*. Additionally, the capabilities presented herein will allow explorations of other clinically-relevant phenomena, such as collagen fiber crosslinking in replacement valvular biomaterials and collagen calcification in heart valve conditions, and the extent to which these permanent microstructural changes impair collagen fiber reorientation in response to mechanical loading. Similar investigations could inform therapeutic efforts such as the synthesis of the collagen ECM within tissue engineered constructs and the development of multi-scale structure-based computational models [10, 72]. Regarding modeling, the load-dependent quantifications provided by the integrated biaxial pSFDI instrument may be incorporated into novel constitutive models of tissue level behavior to allow predictions of a range of tissue mechanics based on the underlying microstructure [94]. This ability to predict mechanics from microstructure could have powerful applications in both biomaterials' selection and tissue engineering applications.

4.4 Conclusion

This study contributes to the fields of biological tissue imaging and biomechanics, with the contributions summarized as follows: (i) development of a novel integrated instrument combining a pSFDI system with a biaxial mechanical tester for load-dependent microstructural quantifications; (ii) verification of the integrated opto-mechanical instrument through imaging on bovine tendon tissue samples; (iii) presentation of the local and bulk microstructural properties of collagen fibers in the representative MVAL tissue samples under various biaxial loading conditions, providing examples of the unique microstructural quantification capabilities of the integrated opto-mechanical instrument. Following this presentation of results, we provided a transparent assessment of the strengths and weaknesses of the system. We have also discussed future paths to remediate the system's shortcomings alongside research extensions that could improve the diagnosis and treatment of collagenous tissue diseases through integrated mechanical and microstructural studies.

Supplementary Material

Refer to Web version on PubMed Central for supplementary material.

Acknowledgments

Supports from the American Heart Association Scientist Development Grant (SDG) Award (16SDG27760143), the Presbyterian Health Foundation Team Science Grants (C5122401), and the Oklahoma Center for the Advancement of Science and Technology (OCAST) Health Research program (HR-18-002) are gratefully acknowledged. CHL was in part supported by the institutional start-up funds from the School of Aerospace and Mechanical Engineering (AME) and the institutional research funding through the Faculty Investment Program from the Research Council and IBEST-OUHSC Interdisciplinary Funding at the University of Oklahoma. We also acknowledge Zachary Schuermann, Donnie Robinson, Keaton Mullenix, and Octavio Serrano for their assistance in the early development of the pSFDI system in the AME Mechanical Engineering Senior Design (capstone) project.

Appendix A:: Overview on the Birefringent Collagen Scattering Theory and Derivation of the pSFDI Intensity Relationship (Eq. (1))

In this Appendix, we describe the polarization of light as it passes through the pSFDI system. In that process, we derive the Fourier cosine series form used to fit the reflected intensity curves (Eq. (1)) and relating the sample's optical properties to the Fourier fitting terms.

To illustrate changes to light polarization in the pSFDI system, we employ a standard Stokes/Mueller approach wherein the intensity and polarization state of light is contained within a 4×1 Stokes vector [**S**]. The first element of [**S**] denotes the light intensity and the subsequent three elements represent the light polarization. In the system, the action of each optical component is represented by its respective Mueller matrix [$\mathbf{M}^{4\times4}$]. At each interface, the incident Stokes vector is multiplied by the acting component's Mueller matrix to yield a modified Stokes vector describing *the light after interaction*. For simplicity, the optical behavior of any system can be condensed via multiplication of the sequential Mueller matrices to reduce to a single system matrix. For example, the entire polarization behavior of the pSFDI system, considering a local reference frame and a polarization angle $\theta_{polarizer}$, can be expressed by

$$[\mathbf{S}_{out}] = \left[\mathbf{M}_{pSFDI}\left(\theta_{fiber}, \theta_{polarizer}\right)\right][\mathbf{S}_{in}], \tag{A1}$$

where [$\mathbf{S}_{in}$] and [$\mathbf{S}_{out}$] denote the Stokes vectors of the incident and output light, respectively, and [$\mathbf{M}_{pSFDI}$] is the Mueller matrix describing the behavior of the pSFDI system associated with polarizer transmission axis at $\theta_{polarizer}$ and the sample with a fiber angle of θ_{fiber}. To derive the complete behavior of the pSFDI system, we can decompose the Mueller matrix into constituent components, i.e.,

$$\left[\mathbf{M}_{pSFDI}\left(\theta_{fiber}, \theta_{polarizer}\right)\right] = \left[\mathbf{M}_{pol}\left(-\theta_{polarizer}\right)\right]\left[\mathbf{M}_{sample}\left(\theta_{fiber}\right)\right] \left[\mathbf{M}_{pol}\left(\theta_{\text{polarizer}}\right)\right], \tag{A2}$$

where [$\mathbf{M}_{pol}(\theta_{polarizer})$] denotes the Mueller matrix of the linear polarizer at angle $\theta_{polarizer}$, and [$\mathbf{M}_{sample}(\theta_{fiber})$] is the Mueller matrix of reflection from the fibrous sample considering fibers with angle θ_{fiber}. Note, as light passes through the polarizer the second time, $\theta_{polarizer}$ is reversed to account for the reflected reference frame. For mathematical simplicity, we can modify Eq. (A2) by adopting the rotating polarizer as the reference to yield a new Mueller form for the pSFDI system, i.e.,

$$[\mathbf{S}_{out}] = \left[\mathbf{M}_{pol}\left(-\theta_{polarizer}\right)\right]\left[\mathbf{M}_{sample}\left(\theta_{fiber}\right)\right]\left[\mathbf{M}_{pol}\left(\theta_{polarizer}\right)\right][\mathbf{S}_{in}]\,. \tag{A3}$$

To solve this equation, quantifications of the Mueller matrices of the linear polarizer [$\mathbf{M}_{pol}(\theta_{polarizer})$], oriented along the x-axis, and the fibrous sample [$\mathbf{M}_{sample}(\theta_{fiber})$] with fibers/optical anisotropy aligned along the same direction are needed. Thus,

$$[\mathbf{M}_{pol}] = \frac{1}{2}\begin{bmatrix} 1 & 1 & 0 & 0 \\ 1 & 1 & 0 & 0 \\ 0 & 0 & 0 & 0 \\ 0 & 0 & 0 & 0 \end{bmatrix}, \quad [\mathbf{M}_{sample}] = R\begin{bmatrix} 1 & D & 0 & 0 \\ D & 1 & 0 & 0 \\ 0 & 0 & \sqrt{1-D^2}cos(\delta) & \sqrt{1-D^2}sin(\delta) \\ 0 & 0 & \sqrt{1-D^2}sin(\delta) & \sqrt{1-D^2}cos(\delta) \end{bmatrix}, \tag{A4}$$

where R is the average reflectance from the sample, and D and δ are the sample diattenuation and phase retardance, respectively, arising from the fiber geometry and considering principal diattenuation and retardance axes aligned with the x- and y-directions, respectively.

When examining rotations of the sample fibers from the polarizer's reference frame, we first note that the rotations in the fiber angle θ_{fiber} are equivalent to the rotations of $[\mathbf{M}_{sample}]$ by an angle of θ_{fiber}. Furthermore, it is noted that a rotation of the linear polarizer by $\theta_{polarizer}$ is equivalent to a rotation to $[\mathbf{M}_{sample}]$ by an angle of $-\theta_{polarizer}$, when viewed from the polarizer's moving reference frame. Therefore, we arrive at a modified Mueller form, i.e.

$$\begin{aligned} &\left[\overline{\mathbf{M}}_{sample}(\theta_{fiber}, \theta_{polarizer})\right] = \left[\mathbf{R}_{rot}(\theta_{polarizer})\right]\left[\mathbf{R}_{rot}(-\theta_{fiber})\right]\left[\mathbf{M}_{sample}(\theta_{fiber})\right] \\ &\left[\mathbf{R}_{rot}(\theta_{fiber})\right]\left[\mathbf{R}_{rot}(-\theta_{polarizer})\right] \\ &= \left[\mathbf{R}_{rot}(\theta_{polarizer} - \theta_{fiber})\right]\left[\mathbf{M}_{sample}(\theta_{fiber})\right]\left[\mathbf{R}_{rot}(\theta_{fiber} - \theta_{polarizer})\right], \end{aligned} \tag{A5}$$

where $[\mathbf{R}_{rot}]$ is the planar rotation matrix, which takes on the form

$$[\mathbf{R}_{rot}(\theta)] = \begin{bmatrix} 1 & 0 & 0 & 0 \\ 0 & \cos(2\theta) & \sin(2\theta) & 0 \\ 0 & -\sin(2\theta) & \cos(2\theta) & 0 \\ 0 & 0 & 0 & 1 \end{bmatrix}. \tag{A6}$$

By assuming the unpolarized incident light $[\mathbf{S}_{in}] = [1,0,0,0]^T$, and by using Eqs. (A5) and (A6), we can solve for $[\mathbf{S}_{out}]$ according to

$$\frac{[\mathbf{S}_{out}]}{\tau_{sys}} = \begin{bmatrix} \frac{3}{2} + \frac{1}{2}\sqrt{1-D^2}\cos(\delta) + 2D\cos\left(2(\theta_{fiber} - \theta_{polarizer})\right) + \frac{1}{2}\left[1 - \sqrt{1-D^2}\cos(\delta)\right]\cos\left(4(\theta_{fiber} - \theta_{polarizer})\right) \\ \frac{3}{2} + \frac{1}{2}\sqrt{1-D^2}\cos(\delta) + 2D\cos\left(2(\theta_{fiber} - \theta_{polarizer})\right) + \frac{1}{2}\left[1 - \sqrt{1-D^2}\cos(\delta)\right]\cos\left(4(\theta_{fiber} - \theta_{polarizer})\right) \\ 0 \\ 0 \end{bmatrix}, \tag{A7}$$

where τ_{sys} is a systemic coefficient depending on the sample reflectance R, the polarizer attenuation, the aperture of the camera, and other non-birefringent optical modifiers. The first term in [95] describes the intensity I_{out} captured by the pSFDI system, which can be represented by a 3-term Fourier cosine series as provided in Eq. (1).

This form allows a quantification of the sample's fiber orientation via Fourier fitting of the experimental intensity data. It is important to note how the sample optical properties, i.e., D and δ, are implicitly embedded in the Fourier coefficients, i.e.,

$$a_0 = 1 + \frac{1}{2}\sqrt{1 - D^2}\cos(\delta),\ a_2 = 2D, \text{ and } a_4 = \frac{1}{2}\left[1 - \sqrt{1 - D^2}\cos(\delta)\right]; \tag{A8}$$

or equivalently

$$D = \frac{a_2}{a_2 + a_4},\ \delta = \cos^{-1}\left(\frac{a_0 - 3a_4}{\sqrt{(a_0 + a_4)^2 - a_2^2}}\right). \tag{A9}$$

By clarifying the relationships between sample diattenuation, retardance, and the three Fourier terms, we establish the basis and validity of the Fourier approximation provided in Eq. (1).

Remark A1: The light reflection at the sample interface was not considered in the Mueller formulation described in Eq. (A5). Because the Mueller matrix [$\mathbf{M}_{sample}$] of a fibrous tissue sample is equivalent in both transmission and reflection modes, leading to the same form of I_{out}, it is trivial to consider reflection of the light coordinate system at the sample interface. If interested, the reader is encouraged to follow the aforementioned approach with inverted [$\mathbf{R}_{rot}$] to consider reflection at the sample interface and derive the same form for I_{out}.

Appendix B:: SFDI theory and Derivation of the AC Image Penetration Depth Relationship

SFDI is a near-infrared planar imaging technique that enables rapid quantification of the tissue properties over a broad FOV. Although SFDI has been widely used towards the quantification of the tissue's optical properties and oxygenation biomarkers [96, 97], our study implements SFDI to *modulate the depth* of our microstructural investigations [98]. Our implementation of SFDI entails a projection of three spatially-modulated unidimensional sinusoidal intensity patterns over a large region (cm-scale). The patterns share the desired spatial frequency f_x, but each exhibits a unique linear phase shift of 0°, 120°, and 240°. The reflected images from each projection pattern are then sequentially captured by a CCD camera and denoted as pixelwise $I_{0°}$, $I_{120°}$, and $I_{240°}$, named according to the respective phase shift of the projection. Then, the pixel-wise intensities extracted from the images are combined according to two conventions: the DC intensity I_{DC} which provides equal weighting for each reflected photon by representing the conventional diffuse reflectance

image, and the AC intensity I_{AC}, which emphasizes the differences between the spatially-modulated intensity patterns $I_{0°}$, $I_{120°}$, and $I_{240°}$:

$$I_{DC} = \frac{I_{0°} + I_{120°} + I_{240°}}{3},\ I_{AC} = \frac{\sqrt{2}}{3}\sqrt{(I_{0°} - I_{120°})^2 + (I_{120°} - I_{240°})^2 + (I_{240°} - I_{0°})^2}. \quad \text{(B1)}$$

Due to photon absorption and scattering events within the sample, both DC and AC spatial intensity maps (or images) predominantly contain information above an effective penetration depth δ_{eff}^{DC} or δ_{eff}^{AC}. These two penetration depths correspond to the positions, where the intensity of electromagnetic radiation inside a sample, as measured by the respective convention in Eq. (B1), falls to $1/e \approx 37\%$ of its incident value. Here, e is the Euler number and the light attenuation rate is described by the Beer-Lambert law [99]. Similar to typical planar projections, δ_{eff}^{DC} exhibits a simple dependence on the sample optical properties according to

$$\delta_{eff}^{DC} = \frac{1}{\sqrt{3\mu_a(\mu_a + \mu_s')}}. \quad \text{(B2)}$$

More specifically, the DC penetration is solely limited by the photons' ability to penetrate the sample, and it is quantified by the tissue bulk optical properties, i.e., the absorption coefficient μ_a and the reduced scattering coefficient μ'_s. This simple dependence renders the DC convention ineffective for interrogating a given tissue sample *at varied imaging depths*, because the effective depth of the DC image has no dependence on the projected pattern. In contrast, the δ_{eff}^{AC} exhibits a dependence on both the tissue optical properties *and* the spatial frequency f_x of the incident projection pattern according to

$$\delta_{eff}^{AC} = \frac{1}{\sqrt{3\mu_a(\mu_a + \mu_s') + (2\pi f_x)^2}}. \quad \text{(B3)}$$

This multivariate depth dependence arises from two factors: (i) the AC intensity's propensity to capture reflected photons that retain the incident spatial pattern, as reflected in the form of Eq. (B1), and (ii) the dependence of the rate of signal attenuation on the spatial frequency of the incident pattern (Fig. B1a and Fig. B1b). Furthermore, at high spatial frequencies relative to the tissue optical properties, the AC penetration depth depends solely on the spatial frequency of the incident pattern (see Eq. (3)), which provides an approximate image penetration depth *independent* of the sample's optical properties.

If shown to be valid for a class of tissues with known ranges of bulk optical properties, this valuable simplification allows a command of the image penetration depth via the control of f_x associated with the projected patterns. For example, to examine the validity of the imaging depth approximation for the *heart valve leaflets* analyzed in this study, we compared Eqs. (B3) and (3) graphically using the previously-obtained optical properties of μ_a=0.07 mm^{-1} and μ'_s=3.00 mm^{-1} for *tendon tissues*, μ_a=0.08 mm^{-1} and μ'_s=1.96 mm^{-1} for

skin tissues, and μ_a=0.03 mm^{-1} and μ'_s=2.19 mm^{-1} for *pericardial tissues* (Fig. B1c) [100, 101].

Remark B1: Note that the optical properties of the tissues used in this example are taken from similar tissues, because the valve leaflet's properties were not readily found in the existing literature. As shown in Figure B1c, the approximation of the imaging depth by Eq. (3) should theoretically be valid over the projected spatial frequency ranges considered in this study (Fig. 7).

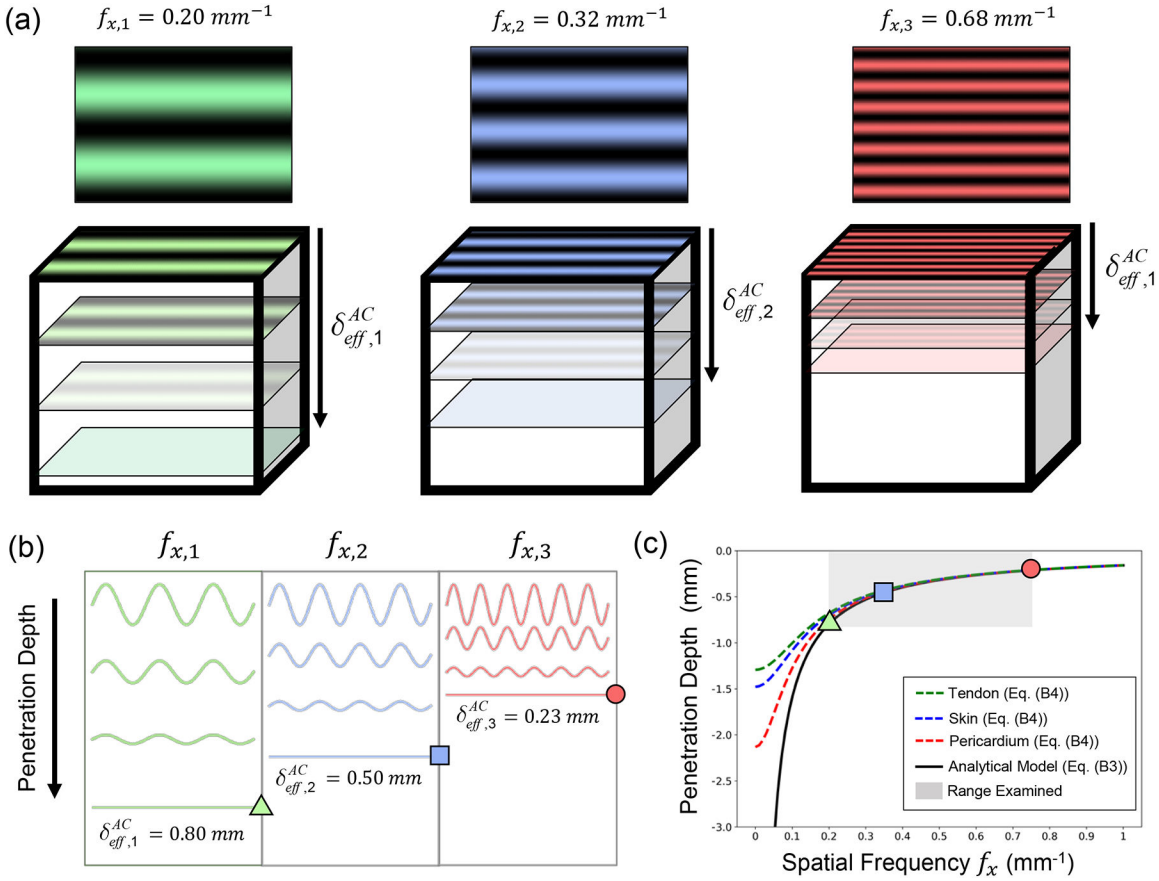

Figure B1 –.

Diagrams exploring the relationship between f_x and δ^{AC}_{eff}. The varied attenuation of three spatial frequency ($f_{x,1–3}$) intensity patterns showing the AC penetration depths ($\delta^{AC}_{eff,1-3}$) according to Eq. (3) from (a) the trimetric view and (b) the side view. (c) Plot comparing estimated penetration depths from the analytical model (Eq. (B3)) for selected tissues [100, 101] and the approximate model (Eq. (3)) with the spatial frequency f_x, highlighting the f_x-range used in this study (cf. Fig. 7).

Appendix C:: Results of Collagen Microstructural Imaging for Another MVAL Tissue Specimen

This appendix presents the quantified collagen fiber architecture of another MVAL tissue specimen under various biaxial tensions (Figs. C1 and C2). The sample preparation and imaging procedures used in this analysis are described in *Study A* (**Section 2.5**) and are the same procedures used in producing the results shown in Figures 5 and 6, albeit considering a different MVAL tissue. Parameters for the distribution fitting, as shown in Figure C2, are included in Table C1.

Table C1 –

Distributions of the CFA in the MVAL Specimen #2 with the bimodal fiber orientation θ_{fiber} fitting, as described by Eq. (4) (cf. Fig. C2a). Anisotropic tissue stretches, pixel sizes for the tissue regions, and descriptive statistics for the DOA distributions (cf. Fig. C2b) with respect to each biaxial loading state.

Bimodal von Mises Distribution Fit to the θ_{fiber} Histograms (cf. FIG. C2A)						
F_C:F_R	μ_1 (deg.)	κ_1 ($\times 10^{-3}$)	w	μ_2 (deg.)	κ_2 ($\times 10^{-3}$)	R^2
0 mN:0 mN (Post-Preconditioning)	72.8	0.73	0.52	166.4	1.03	0.875
1000 mN:1000 mN	71.6	0.12	0.56	166.1	8.42	0.903
250 mN:1000 mN	89.8	1.14	0.53	164.3	2.42	0.813
1000 mN:250 mN	28.3	0.11	0.50	167.0	5.46	0.971

Tissue Stretch			**Pixels in Tissue ROI**	**DOA Descriptive Statistics (cf. Fig. C2b)**		
F_C:F_R	λ_{Circ}	λ_{Rad}		**mean**	**SD**	**skewness**
0 mN:0 mN (Post Preconditioning)	1.00	1.00	545×595	0.034	0.015	0.800
1000 mN:1000 mN	1.19	1.34	649×797	0.075	0.047	1.358
250 mN:1000 mN	1.06	1.38	578×821	0.061	0.032	0.620
1000 mN:250 mN	1.24	1.19	676×708	0.082	0.051	0.678

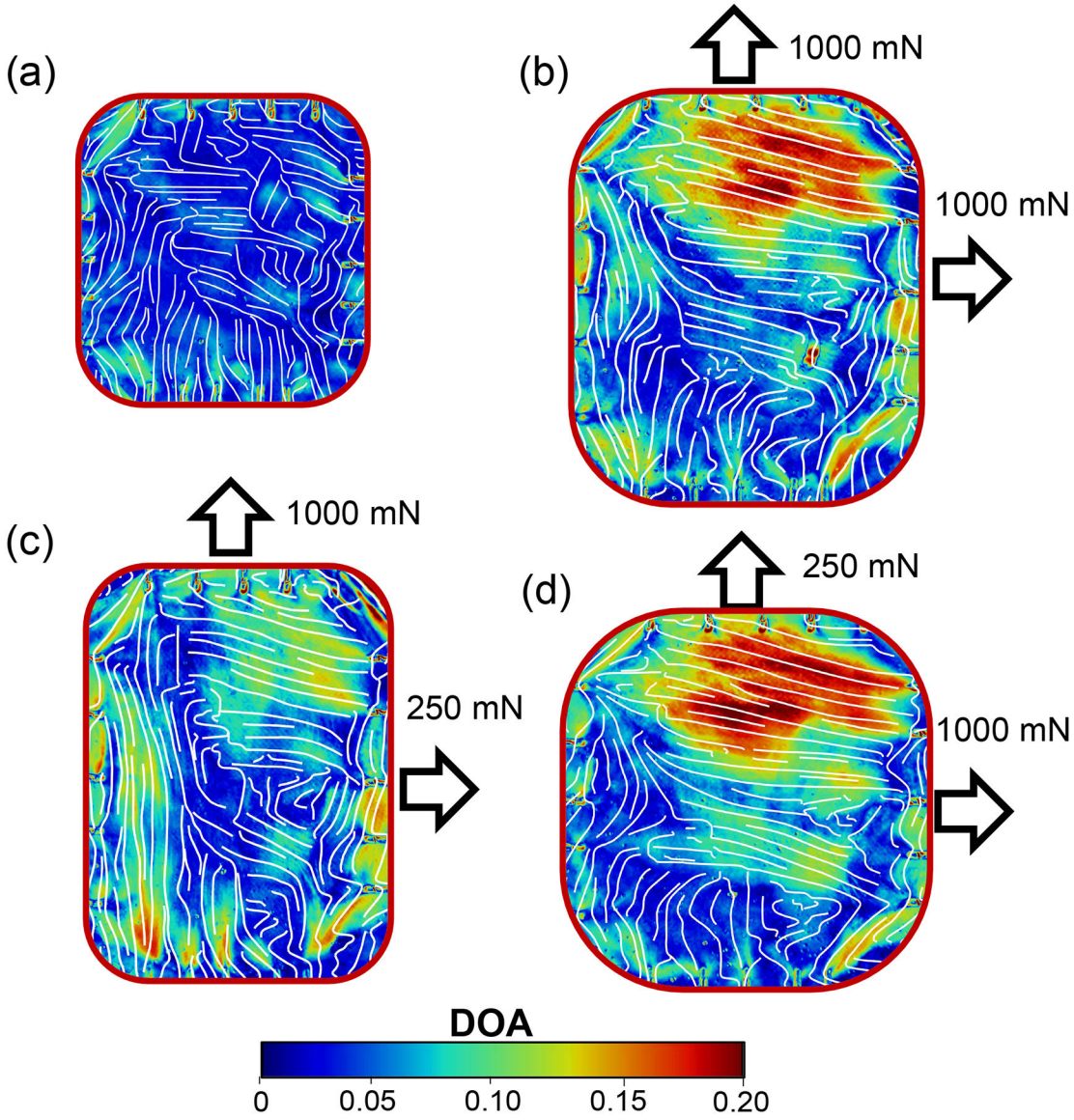

Figure C1 –.

Demonstration of microstructural quantifications of another representative porcine MVAL specimen (thickness=0.87 mm) from the integrated opto-mechanical system (example III): Predictions of θ_{fiber} (white streamlines) and the DOA for the MVAL tissue specimen #2: (a) after preconditioning, and (b)-(d) under various biaxial tensions. Note that the results, as presented in this figure, were from another MVAL tissue specimen different from the one for which the results are presented in Figure 5.).

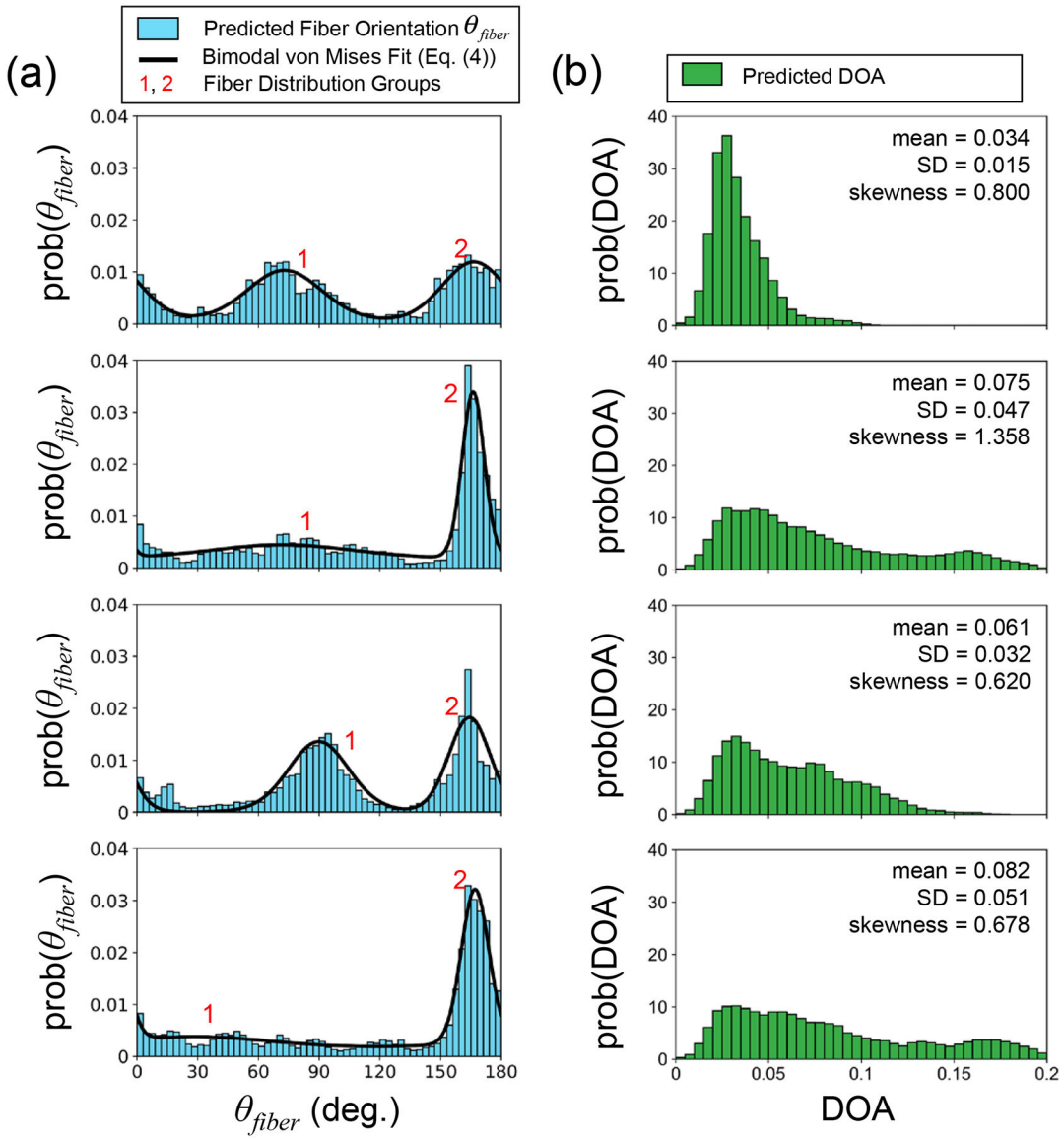

Figure C2 –.

Distributions of θ_{fiber} and DOA predictions from the MVAL biaxial testing in Figure C1: Histograms of (a) the distributions of the predicted θ_{fiber} together with the corresponding bimodal von Mises distribution fit (Eq. (4)), and (b) the predicted DOA. The parameters of the fit are summarized in Table C1, where the distributions were obtained from all the pixels within the ROI. Note that the results, as presented in this figure, were from another representative MVAL tissue specimen different from the one for which the results are presented in Figure 6.).

References

[1]. Jeffery AK, Blunn GW, Archer CW, Bentley G, Three-dimensional collagen architecture in bovine articular cartilage, J. Bone Joint Surg 73(5) (1991) 795–801.

[2]. Quantock AJ, Meek KM, Fullwood NJ, Zabel RW, Scheie's syndrome: The architecture of corneal collagen and distribution of corneal proteoglycans, Can. J. Ophthalmol 28(6) (1993) 266–272. [PubMed: 8299051]

[3]. Liao J, Joyce EM, Sacks MS, Effects of decellularization on the mechanical and structural properties of the porcine aortic valve leaflet, Biomaterials 29(8) (2008) 1065–1074. [PubMed: 18096223]

[4]. Grytz R, Fazio MA, Girard MJA, Libertiaux V, Bruno L, Gardiner S, Girkin CA, Downs JC, Material properties of the posterior human sclera, J. Mech. Behav. Biomed. Mater 29 (2014) 602–617. [PubMed: 23684352]

[5]. Fithian DC, Kelly MA, Mow VC, Material properties and structure-function relationships in the menisci, Clin. Orthop. Relat. Res (252) (1990) 19–31.

[6]. Toshima M, Ohtani Y, Ohtani O, Three-dimensional architecture of elastin and collagen fiber networks in the human and rat lung, Arch. Histol. Cytol 67(1) (2004) 31–40. [PubMed: 15125021]

[7]. Driessen NJB, Bouten CVC, Baaijens FPT, Improved prediction of the collagen fiber architecture in the aortic heart valve, J. Biomech. Eng 127(2) (2005) 329–336. [PubMed: 15971711]

[8]. Gibson T, Kenedi RM, Craik JE, The mobile micro-architecture of dermal collagen: A bio-engineering study, Br. J. Surg 52(10) (1965) 764–770. [PubMed: 5829769]

[9]. Kääb MJ, Ito K, Clark JM, Nötzli HP, Deformation of articular cartilage collagen structure under static and cyclic loading, J. Orth. Res 16(6) (1998) 743–751.

[10]. Fan R, Sacks MS, Simulation of planar soft tissues using a structural constitutive model: Finite element implementation and validation, J. Biomech 47(9) (2014) 2043–2054. [PubMed: 24746842]

[11]. Cox MA, Driessen NJ, Bouten CV, Baaijens FP, Mechanical characterization of anisotropic planar biological soft tissues using large indentation: A computational feasibility study, J. Biomech. Eng 128(3) (2006) 428–436. [PubMed: 16706592]

[12]. Martufi G, Gasser TC, A constitutive model for vascular tissue that integrates fibril, fiber and continuum levels with application to the isotropic and passive properties of the infrarenal aorta, J. Biomech 44(14) (2011) 2544–2550. [PubMed: 21862020]

[13]. Eriksen HA, Satta J, Risteli J, Veijola M, Väre P, Soini Y, Type I and type III collagen synthesis and composition in the valve matrix in aortic valve stenosis, Atherosclerosis 189(1) (2006) 91–98. [PubMed: 16405893]

[14]. Kroon M, Holzapfel GA, A model for saccular cerebral aneurysm growth by collagen fibre remodelling, J. Theor. Biol 247(4) (2007) 775–787. [PubMed: 17482213]

[15]. Horvat N, Virag L, Holzapfel GA, Sorić J, Karšaj I, A finite element implementation of a growth and remodeling model for soft biological tissues: Verification and application to abdominal aortic aneurysms, Comput. Meth. Appl. Mech. Eng 352 (2019) 586–605.

[16]. Gasser TC, Gallinetti S, Xing X, Forsell C, Swedenborg J, Roy J, Spatial orientation of collagen fibers in the abdominal aortic aneurysm's wall and its relation to wall mechanics, Acta Biomater 8(8) (2012) 3091–3103. [PubMed: 22579983]

[17]. Fessel G, Gerber C, Snedeker JG, Potential of collagen cross-linking therapies to mediate tendon mechanical properties, J. Shoulder Elbow Surg 21(2) (2012) 209–217. [PubMed: 22244064]

[18]. Hutson HN, Marohl T, Anderson M, Eliceiri K, Campagnola P, Masters KS, Calcific aortic valve disease is associated with layer-specific alterations in collagen architecture, PLoS ONE 11(9) (2016) e0163858. [PubMed: 27685946]

[19]. Yang B, Lesicko J, Sharma M, Hill M, Sacks MS, Tunnell JW, Collagen fiber orientation mapping with top layer discrimination using polarized light spatial frequency domain imaging (pSFDI) on native heart tissue, Biomedical Optics, Optical Society of America, 2014, p. BM4B. 5.

[20]. Yang B, Brazile B, Jan N-J, Voorhees AP, Sigal IA, Structured polarized light microscopy (SPLM) for mapping collagen fiber orientation of ocular tissues, Proceedings of SPIE Volume 10546, Emerging Digital Micromirror Device Based Systems and Applications X, 2018, p. 105460I.

[21]. Rieppo J, Hallikainen J, Jurvelin JS, Kiviranta I, Helminen HJ, Hyttinen MM, Practical considerations in the use of polarized light microscopy in the analysis of the collagen network in articular cartilage, Microsc. Res. Tech 71(4) (2008) 279–287. [PubMed: 18072283]

[22]. Schriefl AJ, Reinisch AJ, Sankaran S, Pierce DM, Holzapfel GA, Quantitative assessment of collagen fibre orientations from two-dimensional images of soft biological tissues, J. R. Soc. Interface 9(76) (2012) 3081–3093. [PubMed: 22764133]

[23]. Sacks MS, Smith DB, Hiester ED, A small angle light scattering device for planar connective tissue microstructural analysis, Ann. Biomed. Eng 25(4) (1997) 678–689. [PubMed: 9236980]

[24]. Mullaney PF, Dean PN, The small-angle light scattering of biological cells: Theoretical considerations, Biophys. J 10(8) (1970) 764–772. [PubMed: 5475733]

[25]. Liao J, Yang L, Grashow J, Sacks MS, Molecular orientation of collagen in intact planar connective tissues under biaxial stretch, Acta Biomater 1(1) (2005) 45–54. [PubMed: 16701779]

[26]. Chen X, Nadiarynkh O, Plotnikov S, Campagnola PJ, Second harmonic generation microscopy for quantitative analysis of collagen fibrillar structure, Nat. Protoc 7(4) (2012) 654–669. [PubMed: 22402635]

[27]. Tsai M-R, Chiu Y-W, Lo MT, Sun C-K, Second-harmonic generation imaging of collagen fibers in myocardium for atrial fibrillation diagnosis, J. Biomed. Opt 15(2) (2010) 026002. [PubMed: 20459247]

[28]. Zhang Y, Akins ML, Murari K, Xi J, Li M-J, Luby-Phelps K, Mahendroo M, Li X, A compact fiber-optic SHG scanning endomicroscope and its application to visualize cervical remodeling during pregnancy, Proc. Natl. Acad. Sci 109(32) (2012) 12878–12883. [PubMed: 22826263]

[29]. Schriefl AJ, Wolinski H, Regitnig P, Kohlwein SD, Holzapfel GA, An automated approach for three-dimensional quantification of fibrillar structures in optically cleared soft biological tissues, J. R. Soc. Interface 10(80) (2013) 20120760. [PubMed: 23269845]

[30]. Mazzotta C, Hafezi F, Kymionis G, Caragiuli S, Jacob S, Traversi C, Barabino S, Randleman JB, In vivo confocal microscopy after corneal collagen crosslinking, Ocular Surface 13(4) (2015) 298–314.

[31]. Martin C, Sun W, Biomechanical characterization of aortic valve tissue in humans and common animal models, Journal of Biomedical Materials Research Part A 100A(6) (2012) 1591–1599.

[32]. Grauss RW, Hazekamp MG, Oppenhuizen F, van Munsteren CJ, Gittenberger-de Groot AC, DeRuiter MC, Histological evaluation of decellularised porcine aortic valves: matrix changes due to different decellularisation methods, Eur. J. Cardiothorac. Surg 27(4) (2005) 566–571. [PubMed: 15784352]

[33]. Goth W, Yang B, Lesicko J, Allen A, Sacks MS, Tunnell JW, Polarized spatial frequency domain imaging of heart valve fiber structure, Proceedings of SPIE Volume 9710, Optical Elastography and Tissue Biomechanics III, 2016, p. 971019.

[34]. Yang B, Lesicko J, Sharma M, Hill M, Sacks MS, Tunnell JW, Polarized light spatial frequency domain imaging for non-destructive quantification of soft tissue fibrous structures, Biomed. Opt. Express 6(4) (2015) 1520–1533. [PubMed: 25909033]

[35]. Goth W, Potter S, Allen ACB, Zoldan J, Sacks MS, Tunnell JW, Non-destructive reflectance mapping of collagen fiber alignment in heart valve leaflets, Ann. Biomed. Eng 47(5) (2019) 1250–1264. [PubMed: 30783832]

[36]. Longo C, Galimberti M, De Pace B, Pellacani G, Bencini PL, Laser skin rejuvenation: epidermal changes and collagen remodeling evaluated by in vivo confocal microscopy, Lasers Med. Sci 28(3) (2013) 769–776. [PubMed: 22767322]

[37]. Jordan C, Patel DV, Abeysekera N, McGhee CN, In vivo confocal microscopy analyses of corneal microstructural changes in a prospective study of collagen cross-linking in keratoconus, Ophthalmology 121(2) (2014) 469–474. [PubMed: 24183340]

[38]. Wu X, Pankow M, Huang H-YS, Peters K, High-speed polarization imaging of dynamic collagen fiber realignment in tendon-to-bone insertion region, J. Biomed. Opt 23(11) (2018) 116002.

[39]. Tower TT, Neidert MR, Tranquillo RT, Fiber Alignment Imaging During Mechanical Testing of Soft Tissues, Ann. Biomed. Eng 30(10) (2002) 1221–1233. [PubMed: 12540198]

[40]. Alavi SH, Ruiz V, Krasieva T, Botvinick EL, Kheradvar A, Characterizing the collagen fiber orientation in pericardial leaflets under mechanical loading conditions, Ann. Biomed. Eng 41(3) (2013) 547–561. [PubMed: 23180029]

[41]. Gaul RT, Nolan DR, Lally C, Collagen fibre characterisation in arterial tissue under load using SALS, J. Mech. Behav. Biomed. Mater 75 (2017) 359–368. [PubMed: 28787646]

[42]. Schrauwen JTC, Vilanova A, Rezakhaniha R, Stergiopulos N, van de Vosse FN, Bovendeerd PHM, A method for the quantification of the pressure dependent 3D collagen configuration in the arterial adventitia, J. Struct. Biol 180(2) (2012) 335–342. [PubMed: 22728829]

[43]. Voytik-Harbin SL, Roeder BA, Sturgis JE, Kokini K, Robinson JP, Simultaneous mechanical loading and confocal reflection microscopy for three-dimensional microbiomechanical analysis of biomaterials and tissue constructs, Microsc. Microanal 9(1) (2003) 74–85. [PubMed: 12597789]

[44]. Lee C-H, Zhang W, Liao J, Carruthers CA, Sacks JI, Sacks MS, On the presence of affine fibril and fiber kinematics in the mitral valve anterior leaflet, Biophys. J 108(8) (2015) 2074–2087. [PubMed: 25902446]

[45]. Joyce EM, Liao J, Schoen FJ, Mayer JE Jr, Sacks MS, Functional collagen fiber architecture of the pulmonary heart valve cusp, Ann. Thorac. Surg 87(4) (2009) 1240–1249. [PubMed: 19324159]

[46]. Billiar KL, Sacks MS, A method to quantify the fiber kinematics of planar tissues under biaxial stretch, J. Biomech 30(7) (1997) 753–756. [PubMed: 9239558]

[47]. Pham T, Sulejmani F, Shin E, Wang D, Sun W, Quantification and comparison of the mechanical properties of four human cardiac valves, Acta Biomater 54 (2017) 345–355. [PubMed: 28336153]

[48]. Fratzl P, Collagen: structure and mechanics, an introduction, Collagen, Springer2008, pp. 1–13.

[49]. Kannus P, Structure of the tendon connective tissue, Scand. J. Med. Sci. Sports 10(6) (2000) 312–320. [PubMed: 11085557]

[50]. Hielscher AH, Eick AA, Mourant JR, Shen D, Freyer JP, Bigio IJ, Diffuse backscattering Mueller matrices of highly scattering media, Opt. Express 1(13) (1997) 441–453. [PubMed: 19377568]

[51]. Bickel WS, Bailey WM, Stokes vectors, Mueller matrices, and polarized scattered light, Am. J. Phys 53(5) (1985) 468–478.

[52]. Gioux S, Mazhar A, Cuccia DJ, Spatial frequency domain imaging in 2019: Principles, applications, and perspectives, J. Biomed. Opt 24(7) (2019) 071613.

[53]. Maisuradze GG, Thompson DL, Wagner AF, Minkoff M, Interpolating moving least-squares methods for fitting potential energy surfaces: Detailed analysis of one-dimensional applications, J. Chem. Phys 119(19) (2003) 10002–10014.

[54]. Stemper BD, Yoganandan N, Stineman MR, Gennarelli TA, Baisden JL, Pintar FA, Mechanics of fresh, refrigerated, and frozen arterial tissue, J. Surg. Res 139(2) (2007) 236–242. [PubMed: 17303171]

[55]. Woo SL-Y, Orlando CA, Camp JF, Akeson WH, Effects of postmortem storage by freezing on ligament tensile behavior, J. Biomech 19(5) (1986) 399–404. [PubMed: 3733765]

[56]. Foutz TL, Stone EA, Abrams CF III, Effects of freezing on mechanical properties of rat skin, Am. J. Vet. Res 53(5) (1992) 788–792. [PubMed: 1524309]

[57]. Provenzano PP, Vanderby R Jr, Collagen fibril morphology and organization: Implications for force transmission in ligament and tendon, Matrix Biol 25(2) (2006) 71–84. [PubMed: 16271455]

[58]. Franchi M, Trirè A, Quaranta M, Orsini E, Ottani V, Collagen structure of tendon relates to function, Sci. World J 7 (2007) 404–420.

[59]. Kramer KE, Ross CJ, Laurence DW, Babu AR, Wu Y, Towner RA, Mir A, Burkhart HM, Holzapfel GA, Lee C-H, An investigation of layer-specific tissue biomechanics of porcine atrioventricular heart valve leaflets, Acta Biomater 96 (2019) 368–384. [PubMed: 31260822]

[60]. Vesely I, The role of elastin in aortic valve mechanics, J. Biomech 31(2) (1998) 115–123. [PubMed: 9593204]

Health Research Alliance Author Manuscript

[61]. Lee C-H, Carruthers CA, Ayoub S, Gorman RC, Gorman JH III, Sacks MS, Quantification and simulation of layer-specific mitral valve interstitial cells deformation under physiological loading, J. Theor. Biol 373 (2015) 26–39. [PubMed: 25791285]

[62]. Prot V, Skallerud B, Nonlinear solid finite element analysis of mitral valves with heterogeneous leaflet layers, Comput. Mech 43(3) (2009) 353–368.

[63]. Ross CJ, Laurence DW, Wu Y, Lee C-H, Biaxial mechanical characterizations of atrioventricular heart valves, J. Vis. Exp 146 (2019) e59170.

[64]. Humphrey JD, Vawter DL, Vito RP, Quantification of strains in biaxially tested soft tissues, J. Biomech 20(1) (1987) 59–65. [PubMed: 3558429]

[65]. Stella JA, Sacks MS, On the biaxial mechanical properties of the layers of the aortic valve leaflet, J. Biomech. Eng 129(5) (2007) 757–766. [PubMed: 17887902]

[66]. Khoiy KA, Amini R, On the biaxial mechanical response of porcine tricuspid valve leaflets, J. Biomech. Eng 138(10) (2016) 104504.

[67]. Rego BV, Wells SM, Lee C-H, Sacks MS, Mitral valve leaflet remodelling during pregnancy: Insights into cell-mediated recovery of tissue homeostasis, J. R. Soc. Interface 13(125) (2016) 20160709. [PubMed: 27928033]

[68]. Anssari-Benam A, Screen HRC, Bucchi A, Insights into the micromechanics of stress-relaxation and creep behaviours in the aortic valve, J. Mech. Behav. Biomed. Mater 93 (2019) 230–245. [PubMed: 30844614]

[69]. Hadian M, Corcoran BM, Han RI, Grossmann JG, Bradshaw JP, Collagen organization in canine myxomatous mitral valve disease: An x-ray diffraction study, Biophys. J 93(7) (2007) 2472–2476. [PubMed: 17557795]

[70]. Driessen NJB, Cox MAJ, Bouten CVC, Baaijens FPT, Remodelling of the angular collagen fiber distribution in cardiovascular tissues, Biomech. Model. Mechanobiol 7(2) (2008) 93–103. [PubMed: 17354005]

[71]. Fisher NI, Lewis T, Estimating the common mean direction of several circular or spherical distributions with differing dispersions, Biometrika 70(2) (1983) 333–341.

[72]. Aggarwal A, Aguilar VS, Lee C-H, Ferrari G, Gorman JH III, Gorman RC, Sacks MS, Patient-specific modeling of heart valves: From image to simulation, Func. Imaging Model. Heart 7945 (2013) 141–149.

[73]. Holzapfel GA, Niestrawska JA, Ogden RW, Reinisch AJ, Schriefl AJ, Modelling non-symmetric collagen fibre dispersion in arterial walls, J. R. Soc. Interface 12(106) (2015) 20150188. [PubMed: 25878125]

[74]. Grashow JS, Yoganathan AP, Sacks MS, Biaixal stress–stretch behavior of the mitral valve anterior leaflet at physiologic strain rates, Ann. Biomed. Eng 34(2) (2006) 315–325. [PubMed: 16450193]

[75]. Prot V, Skallerud B, Holzapfel GA, Transversely isotropic membrane shells with application to mitral valve mechanics. Constitutive modelling and finite element implementation, Int. J. Numer. Meth. Eng 71(8) (2007) 987–1008.

[76]. May-Newman K, Yin FC, A constitutive law for mitral valve tissue, J. Biomech. Eng 120(1) (1998) 38–47. [PubMed: 9675679]

[77]. Jett SV, Laurence DW, Kunkel RP, Babu AR, Kramer KE, Baumwart R, Towner RA, Wu Y, Lee C-H, Biaxial mechanical data of porcine atrioventricular valve leaflets, Data in Brief 21 (2018) 358–363. [PubMed: 30364794]

[78]. Goth W, Lesicko J, Sacks MS, Tunnell JW, Optical-based analysis of soft tissue structures, Annu. Rev. Biomed. Eng 18 (2016) 357–385. [PubMed: 27420574]

[79]. Lynch HA, Johannessen W, Wu JP, Jawa A, Elliott DM, Effect of fiber orientation and strain rate on the nonlinear uniaxial tensile material properties of tendon, J. Biomech. Eng 125(5) (2003) 726–731. [PubMed: 14618932]

[80]. Lake SP, Miller KS, Elliott DM, Soslowsky LJ, Effect of fiber distribution and realignment on the nonlinear and inhomogeneous mechanical properties of human supraspinatus tendon under longitudinal tensile loading, J. Orth. Res 27(12) (2009) 1596–1602.

[81]. Sacks MS, Smith DB, Hiester ED, The aortic valve microstructure: Effects of transvalvular pressure, J. Biomed. Mater. Res 41(1) (1998) 131–141. [PubMed: 9641633]

[82]. Sun W, Sacks MS, Scott MJ, Effects of boundary conditions on the estimation of the planar biaxial mechanical properties of soft tissues, J. Biomech. Eng 127(4) (2005) 709–715. [PubMed: 16121542]

[83]. Waldman SD, Lee JM, Boundary conditions during biaxial testing of planar connective tissues. Part 1: Dynamic behavior, J. Mater. Sci. Mater. Med 13(10) (2002) 933–938. [PubMed: 15348186]

[84]. Waldman SD, Lee JM, Effect of sample geometry on the apparent biaxial mechanical behaviour of planar connective tissues, Biomaterials 26(35) (2005) 7504–7513. [PubMed: 16002136]

[85]. Laurence DW, Ross CJ, Jett SV, Johns CH, Echols AL, Baumwart R, Towner RA, Liao J, Bajona P, Wu Y, Lee C-H, An investigation of regional variations in the biaxial mechanical properties and stress relaxation behaviors of porcine atrioventricular heart valve leaflets, J. Biomech 83 (2019) 16–27. [PubMed: 30497683]

[86]. May-Newman K, Yin FC, Biaxial mechanical behavior of excised porcine mitral valve leaflets, Am. J. Physiol. Heart Circ. Physiol 269(4) (1995) H1319–H1327.

[87]. Jett SV, Laurence DW, Kunkel RP, Babu AR, Kramer KE, Baumwart R, Towner RA, Wu Y, Lee C-H, An investigation of the anisotropic mechanical properties and anatomical structure of porcine atrioventricular heart valves, J. Mech. Behav. Biomed. Mater 87 (2018) 155–171. [PubMed: 30071486]

[88]. Fan R, Bayoumi AS, Chen P, Hobson CM, Wagner WR, Mayer JE Jr, Sacks MS, Optimal elastomeric scaffold leaflet shape for pulmonary heart valve leaflet replacement, J. Biomech 46(4) (2013) 662–669. [PubMed: 23294966]

[89]. Sacks MS, Biaxial mechanical evaluation of planar biological materials, J. Elast 61(1) (2000) 199.

[90]. Sacks MS, Sun W, Multiaxial mechanical behavior of biological materials, Annu. Rev. Biomed. Eng 5(1) (2003) 251–284. [PubMed: 12730082]

[91]. Slazansky M, Polzer S, Man V, Bursa J, Analysis of accuracy of biaxial tests based on their computational simulations, Strain 52(5) (2016) 424–435.

[92]. Lee C-H, Laurence DW, Ross CJ, Kramer KE, Babu AR, Johnson EL, Hsu M-C, Aggarwal A, Mir A, Burkhart HM, Mechanics of the tricuspid valve—From clinical diagnosis/treatment, in-vivo and in-vitro investigations, to patient-specific biomechanical modeling, Bioengineering 6(2) (2019) 47.

[93]. Khoiy KA, Asgarian KT, Loth F, Amini R, Dilation of tricuspid valve annulus immediately after rupture of chordae tendineae in ex-vivo porcine hearts, PLoS ONE 13(11) (2018) e0206744. [PubMed: 30408050]

[94]. Liang L, Liu M, Sun W, A deep learning approach to estimate chemically-treated collagenous tissue nonlinear anisotropic stress-strain responses from microscopy images, Acta Biomater 63 (2017) 227–235. [PubMed: 28939354]

[95]. Schechter MA, Southerland KW, Feger BJ, Linder D Jr, Ali AA, Njoroge L, Milano CA, Bowles DE, An isolated working heart system for large animal models, J. Vis. Exp (88) (2014).

[96]. Weinkauf C, Mazhar A, Vaishnav K, Hamadani AA, Cuccia DJ, Armstrong DG, Near-instant noninvasive optical imaging of tissue perfusion for vascular assessment, J. Vasc. Surg 69(2) (2019) 555–562. [PubMed: 30292608]

[97]. Yafi A, Muakkassa FK, Pasupneti T, Fulton J, Cuccia DJ, Mazhar A, Blasiole KN, Mostow EN, Quantitative skin assessment using spatial frequency domain imaging (SFDI) in patients with or at high risk for pressure ulcers, Lasers Surg. Med 49(9) (2017) 827–834. [PubMed: 28586092]

[98]. Bodenschatz N, Krauter P, Liemert A, Wiest J, Kienle A, Model-based analysis on the influence of spatial frequency selection in spatial frequency domain imaging, Appl. Opt 54(22) (2015) 6725–6731. [PubMed: 26368086]

[99]. Swinehart DF, The Beer-Lambert law J. Chem. Educ 39(7) (1962) 333.

[100]. Shuaib A, Characterizing Optical Properties in Fibrous Tissues, University of Missouri--Columbia, 2011.

[101]. Sandell JL, Zhu TC, A review of in-vivo optical properties of human tissues and its impact on PDT, J. Biophotonics 4(11-12) (2011) 773–787. [PubMed: 22167862]

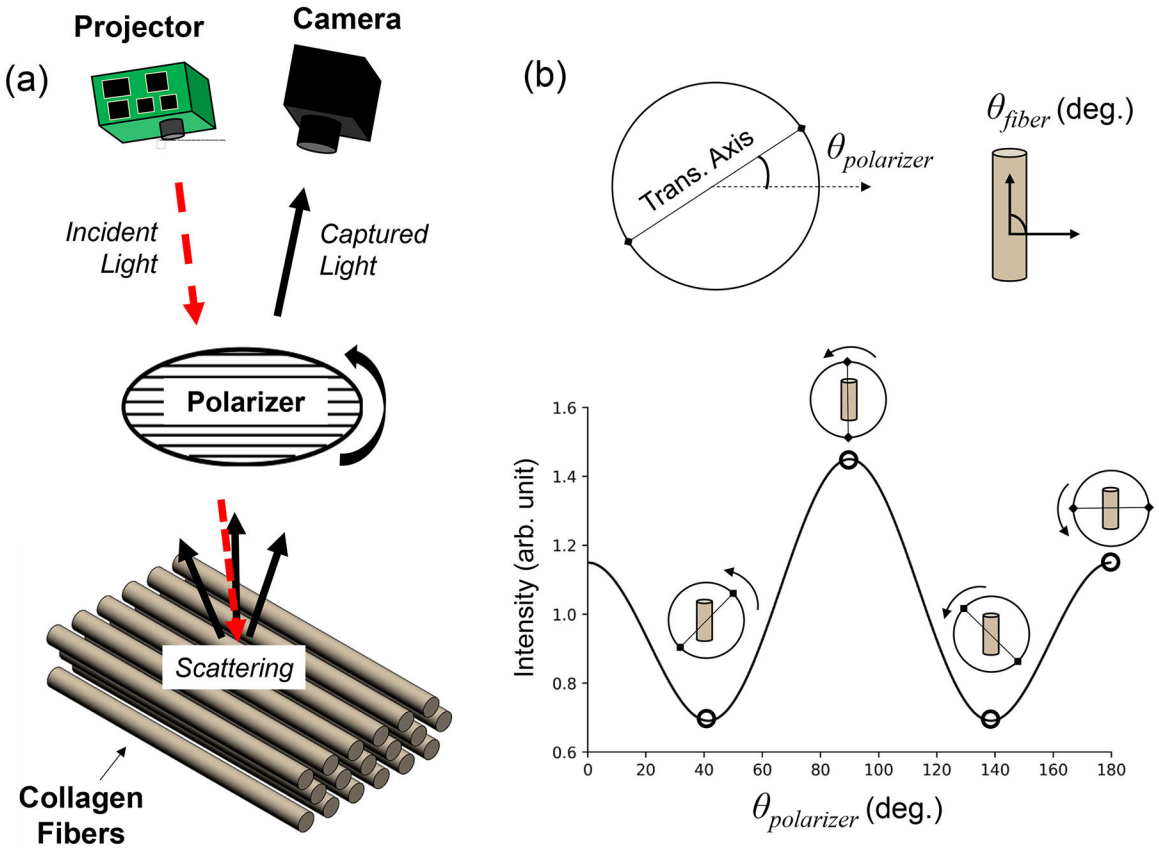

Figure 1 –.

(a) Schematic of a co-polarized pSFDI system, showing the optical components, the *passage of light*, and the scattering from the fibrous tissue microstructure. (b) An illustration of the birefringent reflected intensity response (Intensity vs. $\theta_{polarizer}$) for an example fiber with an orientation angle θ_{fiber}=90° and a polarizer angle $\theta_{polarizer}$ defined on the polar axis with the same reference.

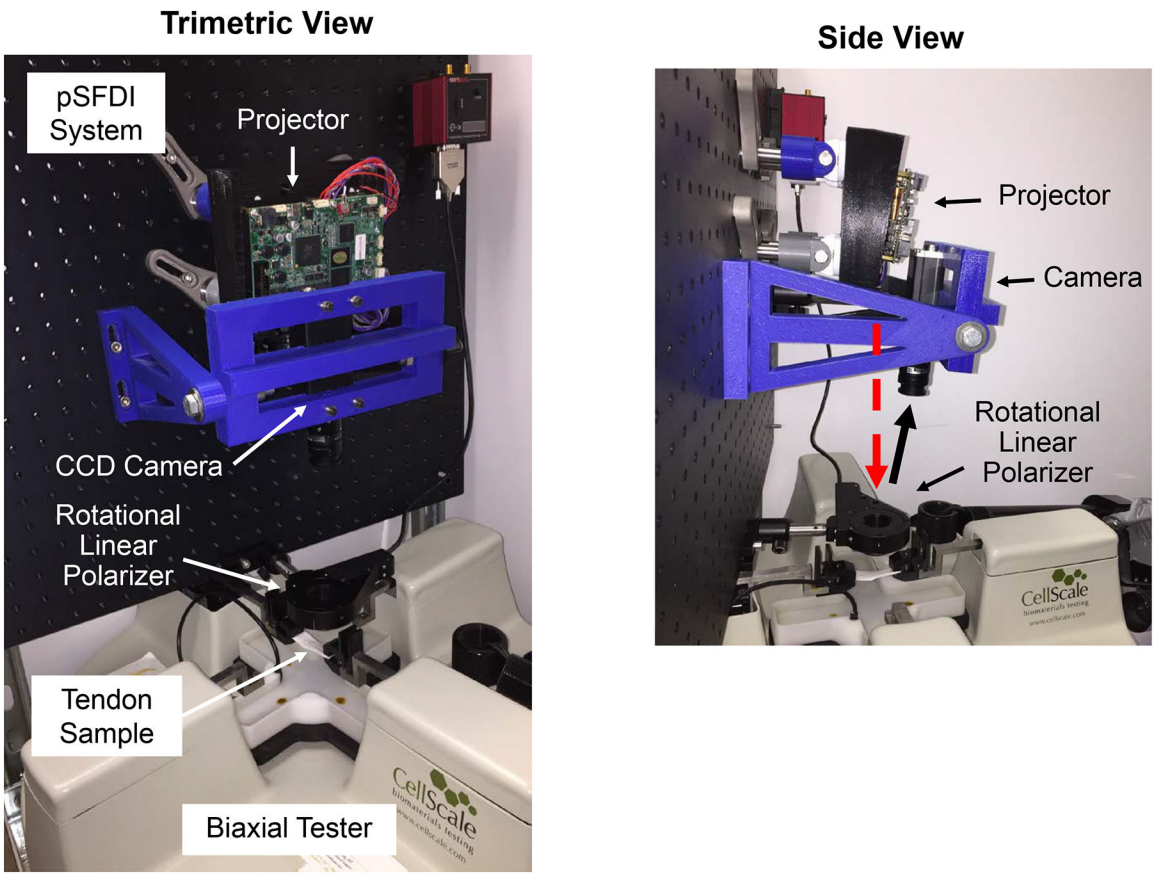

Figure 2 –.

Trimetric and side views of the integrated opto-mechanical system. The arrows in the side view indicate the passage of light through the system using the co-polarized setup.

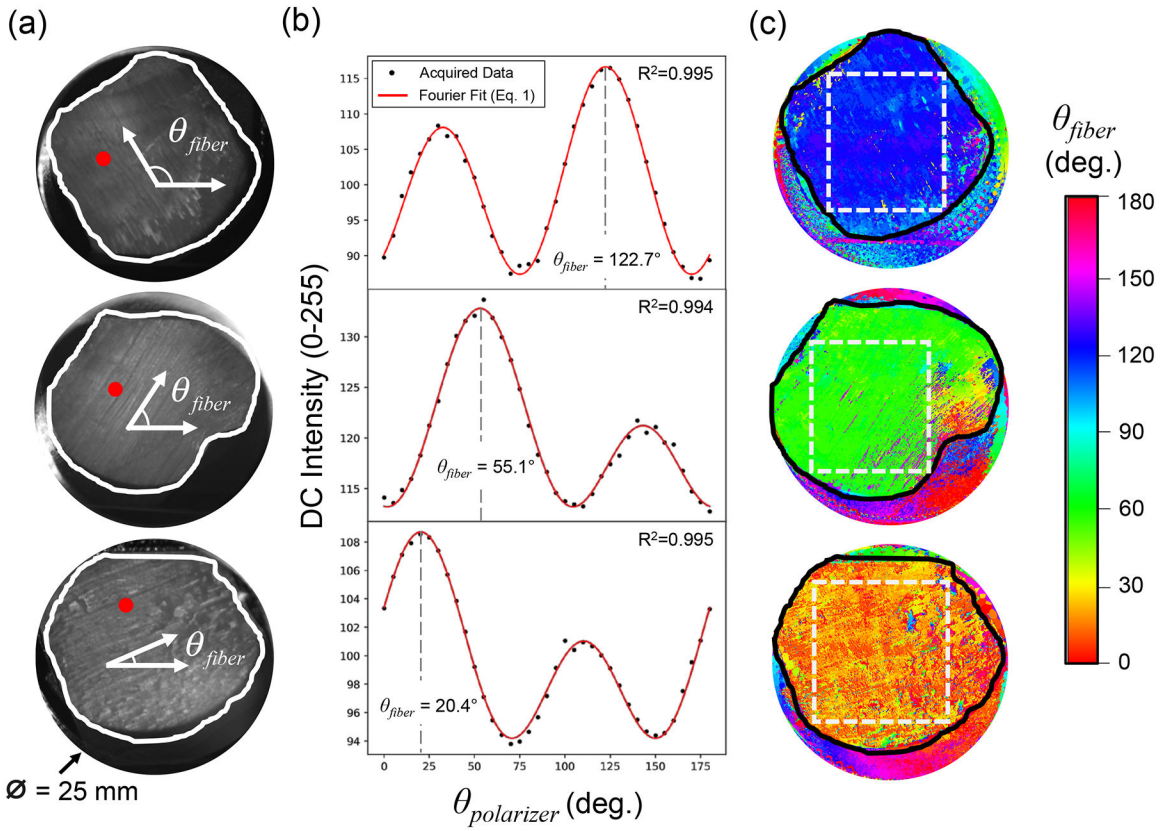

Figure 3 –.

Microstructural quantifications from the pSFDI system: (a) DC intensity images for three bovine tendon tissue specimens, with the expected θ_{fiber} according to the tendon's preferential axial direction, i.e., 122.7° (top), 55.1° (middle), and 20.4° (bottom). Red circles denote the single-pixel locations associated with (b) DC intensity responses, together with the 3-term Fourier series fit (Eq. (1)) for quantifying θ_{fiber}; (c) colormaps of the predicted θ_{fiber} associated with each tendon tissue sample. Rectangle outlined in dashed white lines denotes the area of averaging (cf. Section 3.1). Note that pixel intensities in (b) were stored as unsigned-8-bit integers (range 0–255).

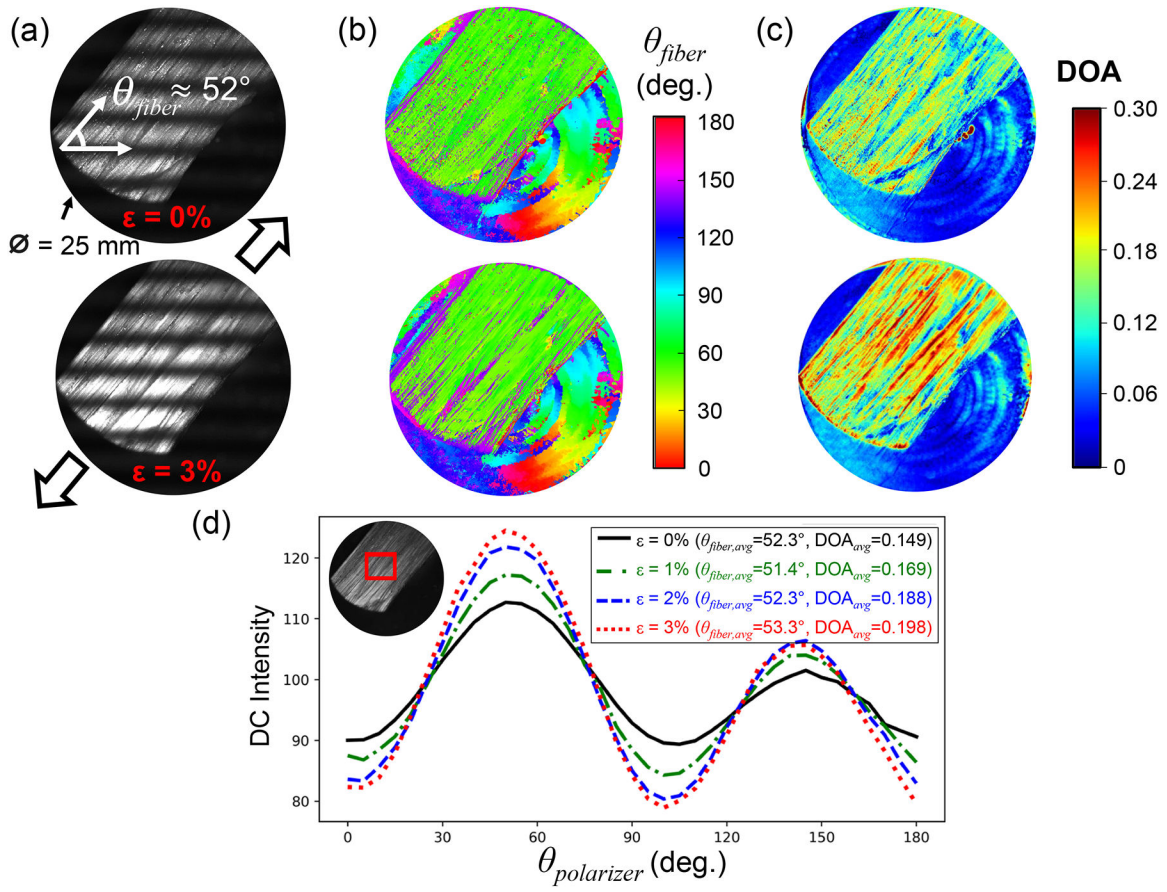

Figure 4 –.

Demonstration of microstructural quantifications from the integrated opto-mechanical system (example I): (a) Experimental raw images of one bovine tendon tissue specimen (thickness=1.25 mm), and the predictions of (b) θ_{fiber} and (c) the degree of optical anisotropy (DOA) at 0% and 3% longitudinal strain ε. (d) Predicted DC intensity responses obtained by spatially averaging over the region outlined by the red rectangle, as shown in the inlet, of the bovine tendon tissue specimen subjected to 0%, 1%, 2%, and 3% longitudinal strains. Note that pixel intensities in (d) were stored as unsigned-8-bit integers (range 0–255).

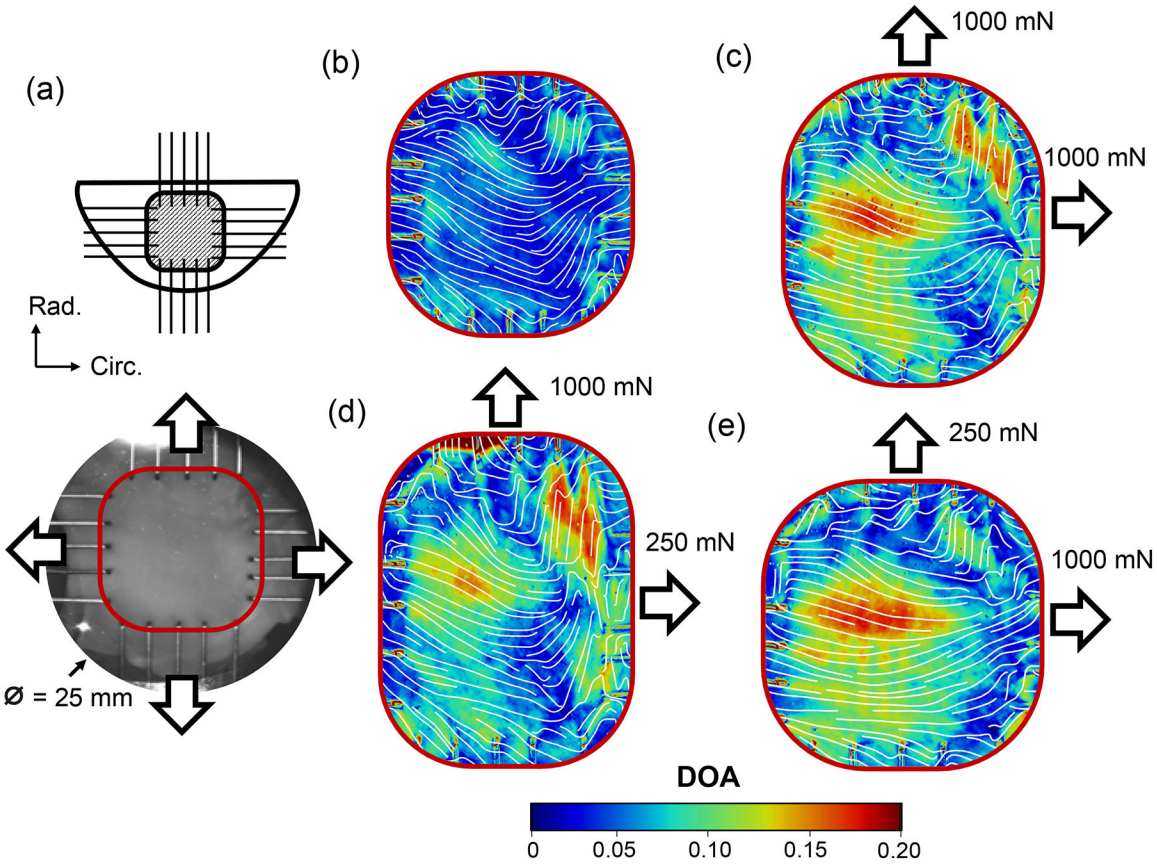

Figure 5 –.

Demonstration of microstructural quantifications from the integrated opto-mechanical system (example II): (a) Schematic of the representative porcine MVAL specimen (thickness=0.75 mm) mounted to the BioTester and the DC image showing the biaxially-loaded region (Circ.: tissue's circumferential direction, Rad.: tissue's radial direction). Predictions of θ_{fiber} (white streamlines) and the DOA for the MVAL tissue specimen #1: (b) after preconditioning, and (c)-(e) under various biaxial loads.

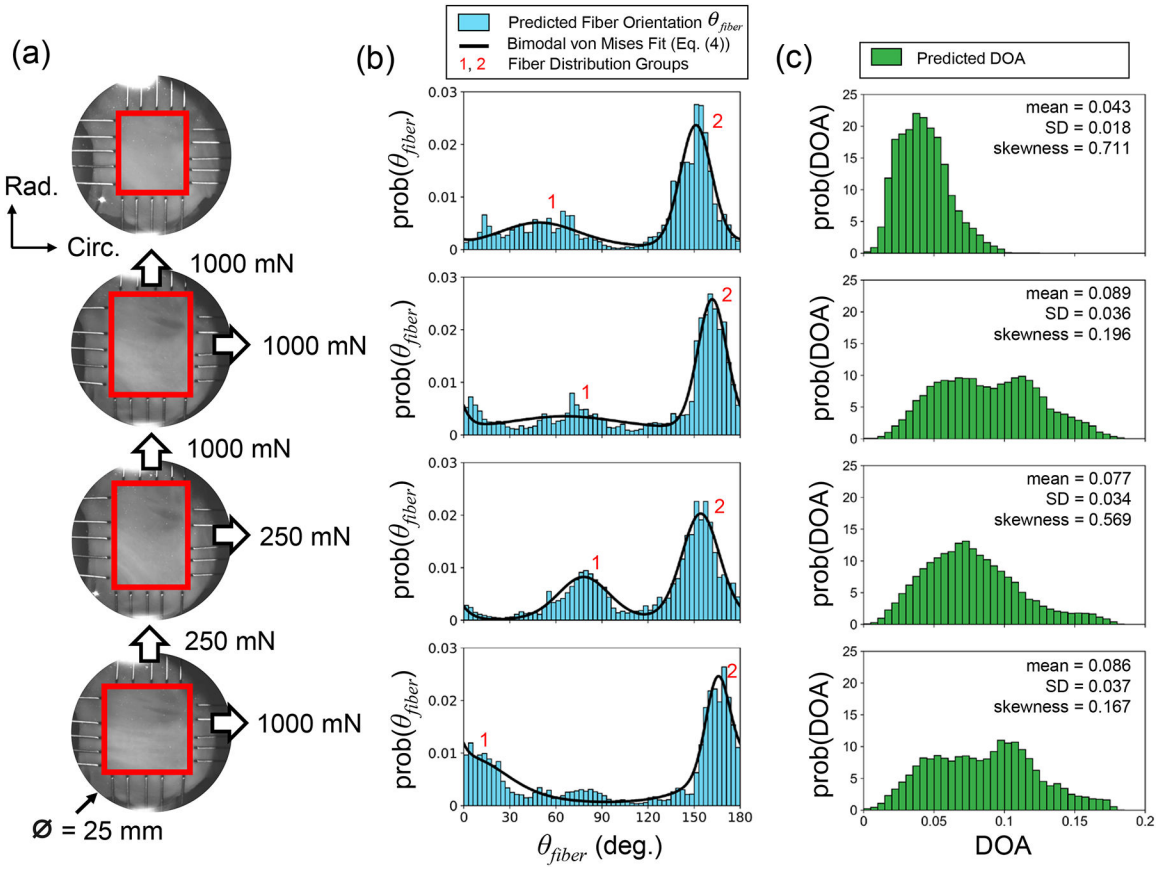

Figure 6 –.

Distributions of θ_{fiber} and DOA predictions from the MVAL biaxial testing in Figure 5: (a) Testing image of the MVAL with the region of interest (ROI) outlined by red rectangles and biaxial loads labeled. Histograms of (b) the distributions of the predicted θ_{fiber} together with the corresponding bimodal von Mises distribution fit (Eq. (4)), and (c) the predicted DOA. The parameters of the fit are summarized in Table 1, where the distributions were obtained from all the pixels within the ROI.

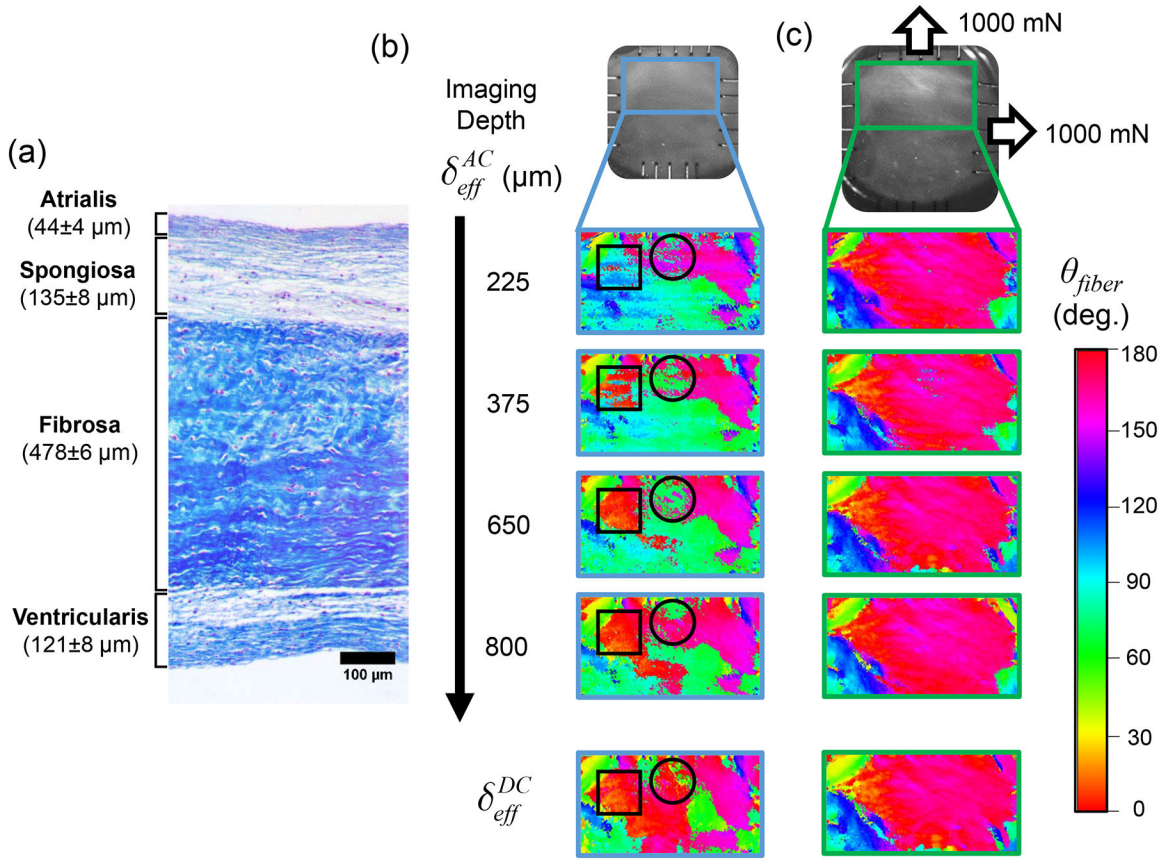

Figure 7 –.

Depth-modulated microstructural predictions from the integrated opto-mechanical system. (a) Histological image illustrating the four morphologically distinct layers of a typical porcine MVAL tissue (image modified from [87]). Predictions of θ_{fiber} from the AC intensities for a representative porcine MVAL tissue sample (thickness=0.87 mm) at various penetration depths associated with different spatial frequencies f_x, as determined by Eq. (3); (b) after preconditioning, and (c) under equibiaxial tension loading of 1000 mN in both the circumferential and radial directions. Predictions from the DC intensities (bottom) are also included to compare the orientation predictions extracted from the "*entire*" optical thickness.

Table 1 –

Comparison of existing collagen fiber quantification techniques [19–21, 26–28, 30, 31].

	polarized Spatial Frequency Domain Imaging (pSFDI)	**Quantitative-Polarized Light Microscopy (Q-PLM)**
Imaging Time	Order of minutes, potentially shorter with improved hardware and lower resolution	Single image capture in seconds, usually requires images at various polarizations
Capture Method	Series of intensity images with varied projection pattern and polarization state	Arbitrarily magnified image capture at varied polarization states
Field of View (FOV)	Varies by lens, as large as desired, on a typically order of cm	Varies by lens (on a typically order of μm-mm)
Resolution	Dictated by pixel-size of images and number of polarization states captured	Varies by lens used, sample thickness, and number of polarization states captured
Contrast Mechanism	Birefringence of collagen fiber structure, reflectance-based	Birefringence of collagen fiber structure, transmission-based, often enhanced via stain

	Small Angle Light Scattering Techniques (SALS and SAXS)	**Second Harmonic Generation (SHG) Microscopy**
Imaging Time	Order of hours, depends on the size and the desired resolution	Single image capture on order of minutes
Capture Method	Rasterized scanning with image capture at each raster point	Second harmonic frequency generation and capture at each pixel of final image
FOV	As large as desired, typically at the cm-scale for SALS, smaller for SAXS due to time limitations	Initial images on the order of μm; reconstructed images on the order of 100 μm
Resolution	Dependent on the depth-averaged diffusion, incident beam size and wavelength (SALS: ~μm, SAXS: ~nm)	High resolution, capable of resolving individual collagen fibrils
Contrast Mechanism	Anisotropic light scattering signatures of fibrous structures extracted from transmitted light profiles	Birefringent molecular hyperpolarizability among fibers/ fibrils alongside frequency-doubling nonlinear phenomena

	Confocal Microscopy	**Histological Methods**
Imaging Time	Depends on the specimen size and desired resolution, typically seconds to minutes	Single image capture on the order of milliseconds
Capture Method	Laser scanning approach with intensity captured at various tomographic planes	Traditionally analyzed with standard microscopy methods; intensity image capture
FOV	Can achieve a mm-scale through laser-scanning methods, otherwise at the μm-scale	Typical images on the order of μm, depends on the associated eyepiece and objective lenses
Resolution	A μm-scale in both the spatial and transmural directions, through restriction of captured light to focal plane	Depends on the magnification of the associated objective; capable of resolving individual collagen fibrils
Contrast Mechanism	Reflectance and absorption differences between structures, adjustable focal plane through a pinhole restriction	Stains bind to collagen fiber structures and increase visual contrast with surrounding media, changing apparent color in image

Table 2 –

Distributions of the CFA in the MVAL Specimen #1 with the bimodal fiber orientation θ_{fiber} fitting, as described by Eq. (4) (cf. Fig. 6b). Anisotropic tissue stretches, pixel sizes for the tissue regions (cf. red boxes in Figure 6a), and descriptive statistics for the DOA distributions (cf. Fig. 6c) with respect to each biaxial loading state.

Bimodal von Mises Distribution Fit to the θ_{fiber} Histograms (cf. Fig. 6b)						
F_C:F_R	μ_1 (deg.)	κ_1 ($\times 10^{-3}$)	w	μ_2 (deg.)	κ_2 ($\times 10^{-3}$)	R^2
0 mN:0 mN (Post-Preconditioning)	49.1	0.35	0.40	151.1	2.42	0.908
1000 mN:1000 mN	66.0	0.15	0.42	161.8	2.84	0.936
250 mN:1000 mN	78.1	0.92	0.36	154.3	1.66	0.943
1000 mN:250 mN	3.0	0.39	0.67	165.3	4.32	0.938

Tissue Stretch			**Pixels in Tissue ROI**	**DOA Descriptive Statistics (cf. Fig. 6c)**		
F_C:F_R	λ_{Circ}	λ_{Rad}		**mean**	**SD**	**skewness**
0 mN:0 mN (Post Preconditioning)	1.00	1.00	485×415	0.043	0.018	0.711
1000 mN:1000 mN	1.17	1.27	567×527	0.089	0.036	0.196
250 mN:1000 mN	1.06	1.31	514×544	0.077	0.034	0.569
1000 mN:250 mN	1.24	1.11	601×461	0.086	0.037	0.167